Chemical Science

ROYAL SOCIETY OF CHEMISTRY

REVIEW

View Article Online
View Journal | View Issue

Cite this: *Chem. Sci.*, 2026, **17**, 7843

Advances in electrochemical technologies for PFAS destruction

Yuqing Dong,[a] Shuaiyu Gao,[a] Yuelin Zhao,[a] Genban Sun *[a] and Jihong Yu *[ab]

Received 3rd December 2025
Accepted 16th March 2026

DOI: 10.1039/d5sc09459c

rsc.li/chemical-science

Per- and polyfluoroalkyl substances (PFAS) are a class of man-made chemicals extensively employed in industrial processes, with their strong C–F bond energy conferring exceptional stability. However, this stability also leads to bioaccumulation and environmental persistence, posing threats to ecosystems and human health. Conventional physical separation technologies can only concentrate PFAS without completely destroying them. Against this backdrop, electrochemical technology has emerged as one of the most promising strategies for complete PFAS destruction, benefiting from its mild reaction conditions and controllable electron transfer. This review systematically summarizes the research progress on electrochemical PFAS degradation, comprehensively examining the degradation mechanisms and key influencing factors in electrochemical oxidation, reduction, and combined processes. It highlights the crucial roles of density functional theory (DFT) and molecular dynamics (MD) calculations in elucidating interfacial behaviors and atomic-scale C–F bond activation mechanisms. Addressing the bottlenecks of mass transfer limitations and incomplete defluorination encountered in practical applications, this paper prospectively points out the potential of microenvironmental regulation and the development of bifunctional materials for achieving *in situ* deep mineralization. Furthermore, it briefly explores the application prospects of artificial intelligence (AI)-enabled high-throughput screening technologies in accelerating the development of multi-objective electrode materials. Overall, this review constructs a comprehensive research framework spanning from fundamental bond cleavage mechanisms to macroscopic processes and data-driven optimization. It provides systematic strategies for the complete destruction of PFAS and offers theoretical references for the rational design of advanced environmental functional materials.

1 Introduction

Per- and polyfluoroalkyl substances (PFAS) exhibit exceptional thermochemical stability along with hydrophobic and oleophobic properties.[1–3] These characteristics enable their extensive use in chemical manufacturing, electronics, medical devices, textiles, and consumer products.[4,5] However, these same properties confer high environmental persistence and bioaccumulation in natural systems.[6] PFAS residues have now been detected in aquatic environments, atmospheric compartments, and soils across multiple global regions.[7] Consequently, PFAS are recognized as emerging persistent organic pollutants of particular concern in aquatic systems. Epidemiological studies confirm that PFAS exposure induces multi-organ toxicity, affecting the liver, kidneys, thyroid, and other systems.[8] Given their environmental recalcitrance and significant ecotoxicity, PFAS pose systemic threats to ecosystem integrity and public health.[9]

It is reported that approximately 450–2700 tons of perfluorooctane sulfonate (PFOS) enter wastewater systems globally each year.[10] To mitigate environmental and health risks, multiple countries have legislated restrictions on PFAS production and usage.[11] In 2023, China included PFOS in the List of Priority Controlled New Pollutants, stipulating that its import and export will be prohibited starting from 2024, and requiring that PFOS-containing waste be subject to full-process supervision as hazardous waste. Practically, cities like Shanghai have carried out projects to replace firefighting foam and advance drinking water treatment. Through nanofiltration and activated carbon adsorption, the concentration of PFOS in water has been successfully controlled below 0.5 $\mu g\ L^{-1}$. Concurrently, the U.S Environmental Protection Agency has set the limit for perfluorooctanoic acid (PFOA) and PFOS in drinking water at 4 $ng\ L^{-1}$, while Denmark enforces a stricter 2 $ng\ L^{-1}$ threshold in relation to separate PFAS analytes.[12] Significantly, the European Union amended its Persistent Organic Pollutants Regulation in April 2025, tightening unintentional trace contaminant limits for PFOS and its salts to 0.025 $mg\ kg^{-1}$.[13]

---

[a] *Beijing Key Laboratory of Energy Conversion and Storage Materials, College of Chemistry, Beijing Normal University, Beijing 100875, China. E-mail: gbsun@bnu.edu.cn*

[b] *State Key Laboratory of Inorganic Synthesis and Preparative Chemistry, College of Chemistry, International Center of Future Science, Jilin University, Changchun 130012, China. E-mail: jihong@jlu.edu.cn*

Given the extreme environmental persistence and trace-level occurrence of PFAS in contaminated media, developing efficient removal technologies constitutes a critical scientific challenge in environmental remediation.[14]

In conventional PFAS treatment technologies, adsorption methods achieve PFAS enrichment through physicochemical interactions.[15,16] Activated carbon exhibits >90% capture efficiency for long-chain PFAS thanks to its large specific surface area, while functionalized ion-exchange resins enhance adsorption capacity to 120 mg g^{-1}.[17] However, short-chain PFAS remain challenging to remove effectively due to their high aqueous solubility and low adsorption affinity, with competitive anions reducing ion-exchange efficiency by >50%.[18] Additionally, spent adsorbents require energy-intensive thermal regeneration or hazardous waste disposal.[16] Membrane separation technologies leverage molecular exclusion mechanisms, where reverse osmosis (RO) achieves >99% removal efficiency across the PFAS spectrum, and nanofiltration (NF) selectively retains >90% of long-chain PFAS. Their modular design facilitates large-scale water supply applications without chemical additives.[19] Nevertheless, RO consumes 3–10 kW h per ton of water and generates concentrated PFAS waste streams, with membrane fouling causing 40–70% flux decline. NF demonstrates limited efficacy for short-chain PFAS, accompanied by substantial membrane replacement costs. Recently developed destructive technologies, though proven for PFAS degradation in laboratory settings, face significant practical limitations. Current methods face significant hurdles: sonolysis is energy-intensive, bioremediation yields less than 10% metabolic efficiency, and photocatalysis suffers from low quantum yields and organic matter interference. These techniques exhibit poor anti-interference capacity in complex aquatic matrices and lack validation at engineering scales, severely constraining their potential for full-scale implementation.[20]

Electrochemical techniques have evolved into a prominent research topic in PFAS degradation studies, thanks to their mild reaction conditions, precisely controllable redox capacity, and particularly its dual functions of pollutant separation and mineralization destruction.[21] Electrocoagulation (EC) achieves indirect adsorption of PFAS through hydroxide flocs formed by the dissolution of metal anodes.[22] Capacitive deionization (CDI), on the other hand, completes molecular-level concentration of PFAS driven by the electrostatic force of the electric double layer.[23] However, EC and CDI can only realize the enrichment and concentration of PFAS, and cannot break their stable C–F bonds. By coupling electrochemical oxidation (EO) and electrochemical reduction (ER) processes, the cleavage of C–F bonds in PFAS can be achieved, ultimately mineralizing them into harmless products such as CO_2 and F^-. EO utilizes strong oxidizing species like hydroxyl radicals ($\cdot$OH) and sulfate radicals ($SO_4^{\bullet-}$) generated by boron-doped diamond (BDD) or Ti_4O_7 anodes, or through a direct electron transfer (DET) mechanism, to efficiently degrade typical PFAS such as PFOA and PFOS. ER triggers H/F exchange reactions through DET or *via* hydrated electrons (e_{aq}^-) and hydrogen radicals ($\cdot$H) generated at the cathode, gradually defluorinating to form low-fluorinated products.[24] Current research frontiers focus on developing magnetic electrode materials to enable efficient recovery of adsorbents and the *in situ* coupled design of oxidation-reduction bifunctional electrodes. Meanwhile, benefiting from the development of advanced characterization techniques, the understanding of multi-scale mechanisms from atomic interfacial reaction pathways to macroscopic kinetics continues to deepen.[25] Despite the significant advantages exhibited by electrochemical technology, there remains an urgent need for systematic reviews in this field to clarify three key challenges: the reaction pathways of PFAS degradation by EO and ER, the quantitative laws governing the structure–activity relationships of electrode materials, and the strategies for inhibiting interference from actual water matrices.[26] This will provide theoretical guidance for the engineering application of such technologies.[27]

Meanwhile, this review comprehensively evaluates the efficacy and mechanisms of EO, ER, and their synergistic technologies. In terms of characterization and auxiliary research techniques, the review focuses on multi-scale analytical methods and emerging intelligent auxiliary tools, including microstructure analysis of electrode materials, tracking of interfacial reaction processes, free radical identification, DFT/MD theoretical calculations, and AI-enabled HTS. These combined methods not only help clarify atomic-level reaction pathways but also promote the efficient development of high-performance electrochemical PFAS degradation systems.

This review systematically summarizes the state-of-the-art progress in the electrochemical degradation of PFAS (Fig. 1). To bridge the gap between atomic level interactions and macroscopic performance, this review first highlights the critical roles of multi-scale analytical methods and theoretical calculations, specifically density functional theory (DFT) and molecular dynamics (MD), in unraveling complex interfacial behaviors and C–F bond activation mechanisms. Building upon this fundamental understanding, we comprehensively evaluate the efficacy and governing mechanisms of diverse electrochemical strategies. For EO, we elucidate the synergistic effects of DET and indirect radical oxidation, detailing specific degradation pathways on benchmark anodes alongside key operational parameters. Regarding ER, we systematically unpack the stepwise defluorination mechanisms mediated by DET, $\cdot$H, and

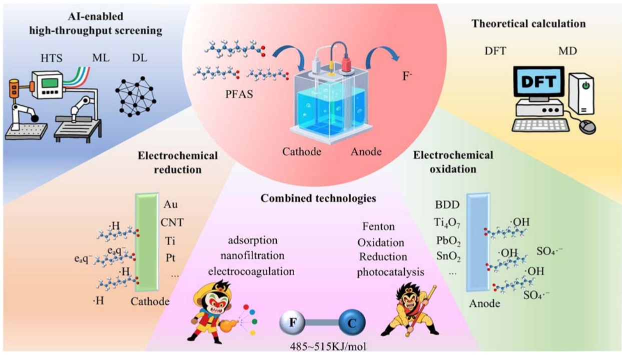

Fig. 1 Schematic diagram of systematic study on electrochemical degradation of PFAS.

e_aq^-, followed by rational design strategies for carbon-based and catalyst-supported cathodes.

Recognizing the inherent limitations of stand-alone processes, we further explore recent advancements in synergistic technologies that couple electrochemistry with adsorption, membrane separation, and photocatalysis. These combined systems demonstrate significant advantages in overcoming mass transfer bottlenecks, reducing specific energy consumption, and enhancing overall defluorination efficiency. Beyond traditional material design, this review incorporates the transformative potential of artificial intelligence (AI)-enabled high-throughput screening (HTS) in establishing a closed-loop framework for the rapid discovery and multi-objective optimization of next-generation electrodes. Finally, we prospectively outline the persistent challenges and emerging opportunities in the field. By advocating for the in-depth integration of electrochemical technologies with separation techniques and data-driven paradigms, this work aims to provide a robust scientific foundation and a forward-looking roadmap for developing highly efficient, practical technologies to ultimately eradicate these recalcitrant "forever chemicals" from the environment.

2 Methodologies of mechanism and pathway investigations

Electrochemical technologies have demonstrated the capability to achieve complete mineralization of PFAS with high economic and environmental compatibility, thereby emerging as a promising research frontier in the field of environmental remediation. This chapter presents a systematic review of the core characterization techniques employed in investigating electrochemical PFAS degradation.[28] The discussion encompasses the theoretical interpretive frameworks integral to this research domain, including: (1) structural and interfacial characterization of electrode materials, (2) quantitative analysis of reaction intermediates, (3) mechanistic elucidation of free radical species, and (4) theoretical calculation method. Collectively, these methodologies enable a multi-scale understanding of electrochemical PFAS degradation by bridging experimental observations with theoretical frameworks, from atomic-level interfacial interactions to macroscopic reaction kinetics. Application of these characterization methodologies facilitates the revelation of degradation pathways, prediction of reaction energetics, and rational design of efficient, sustainable electrochemical technologies for PFAS abatement.[29]

2.1 Characterization of electrode materials

The type and properties of electrode materials are core determinants in the electrochemical degradation of PFAS. Analysis of their electrical conductivity, oxygen evolution potential (OEP), surface reactivity, structural characteristics, and stability provides critical guidance for electrode design. Scanning electron microscopy-energy dispersive spectroscopy (SEM-EDS) enables visual characterization of the microstructure and elemental distribution on electrode surfaces. Successful material synthesis, uniform elemental distribution, and the impact of structural features on catalytic activity can all be validated by SEM-EDS analysis.[30] The in-depth analysis of the surface chemical state and crystal structure of electrode materials relies on X-ray photoelectron spectroscopy (XPS) and X-ray diffraction (XRD). XPS is a key tool for understanding the efficient defluorination mechanism, as it can analyze the electron transfer, adsorption behavior, and intermediate product evolution between electrodes and PFAS. XRD is used to determine the crystal structure of electrode materials and structural changes induced by doping. For example, when Ce^{3+} is doped into Ti_4O_7 electrodes, the shift of XRD diffraction peaks indicates that Ce^{3+} doping leads to lattice distortion and the generation of oxygen vacancies.[31] The characteristic diffraction peaks (111) and (220) of BDD electrodes show an inverse relationship between the full width at half maximum and grain size, which directly affects the electrical conductivity of the electrodes.[32,33] These structural features play a decisive role in the selective adsorption of PFAS.

The characterization of electrochemical activity and interfacial properties of electrodes is primarily achieved through various voltammetric techniques and impedance spectroscopy. The Linear Sweep Voltammetry (LSV) curve, by measuring the electrode potential–current response, accurately defines the working potential window of the electrode and quantifies the OEP, thereby distinguishing the oxidation pathways for PFAS degradation. For instance, the Ti/BDD electrode exhibits an OEP of 2.8 V *vs.* SCE, and its high OEP enables preferential indirect oxidation *via* ·OH generated from water oxidation to mineralize long-chain perfluorocarboxylic acids (PFCAs).[34] Cyclic Voltammetry (CV), through scan rate-dependent analysis, reveals the adsorption mechanism and electron transfer kinetics of PFAS on the electrode surface, which is crucial for evaluating the redox characteristics of electrodes. For example, the hexadecyltrimethylammonium bromide(CTAB)-functionalized CNT electrode shows a characteristic reduction peak of PFOS at −0.58 V *vs.* Ag/AgCl, and the peak current correlates linearly with the scan rate, confirming that cationic surfactants regulate the interfacial electron transfer of PFAS *via* electrostatic adsorption.[35] Electrochemical Impedance Spectroscopy (EIS), by fitting equivalent circuit models, accurately characterizes the charge transfer resistance (R_{ct}) and mass transfer processes at the electrode/solution interface. For instance, the F/Sb co-doped Ti/Sn–Sb/SnO_2–F–Sb electrode reduces R_{ct} to 85 Ω cm^2 by forming Sn–O–F bond defects, enabling efficient electron transfer for PFOS degradation.[36] The interfacial properties of electrodes are critical for PFAS electrochemical degradation. Future designs should balance high OEP, low impedance, and anti-dissolution performance of electrode materials to achieve efficient and stable PFAS mineralization.

2.2 Analysis of reaction intermediates

Precise quantification of defluorination efficiency and identification of intermediate products are key indicators for evaluating PFAS treatment technologies. The fluoride ion-selective electrode (F^-–ISE) has emerged as the preferred method for continuous monitoring of F^- release due to its advantages of simplicity and rapidity. Furthermore, ion chromatography (IC) offers high sensitivity and anti-interference capability, making it particularly suitable for the analysis of complex matrix samples.[37] Liquid chromatography-tandem mass spectrometry (LC-MS/MS), with its superior separation and structural identification capabilities, identifies intermediates by resolving ion peaks. For example, the detection of short-chain PFOS anions in PFOS degradation provides direct evidence of a stepwise chain-shortening mechanism driven by ·OH radical attack on $-CF_2-$ moieties.[38] The detection of intermediates confirms that degradation occurs *via* direct electron transfer-driven decarboxylation and C–F bond cleavage.[39] Nuclear Magnetic Resonance (NMR) spectroscopy provides direct evidence of molecular structural changes during the defluorination process. For instance, ^{19}F NMR analysis reveals a shift in the fluorine signal of the CF_2 groups in PFOA, moving from −119 ppm to −116 ppm, attributed to altered electronic environments after decarboxylation. This signal shift indicates preferential cleavage of the C–F bonds adjacent to the carboxyl group, confirming the occurrence of decarboxylation.[40]

2.3 Free radical identification

Accurate identification of reactive free radicals generated during the electrochemical degradation of PFAS is crucial for elucidating the reaction mechanisms, as these radicals are key intermediates responsible for triggering the cleavage of C–F bonds. Electron Spin Resonance (ESR) spectroscopy, as the standard for direct detection of unpaired electrons, plays a core role in radical identification. The characteristic signals of Cl· and ·OH observed in ESR spectra demonstrate their critical roles in PFOA degradation, where Cl· triggers the initial reaction and ·OH participates in subsequent carbon chain cleavage.[41] Radical quenching experiments indirectly validate the contribution of specific radicals through kinetic intervention. This approach involves introducing selective quenchers into the system and observing changes in degradation efficiency and pathways.[42] The quenching experiments and ESR results corroborate each other, revealing the degradation pathways of PFAS and enabling efficient degradation.

2.4 Theoretical calculation

Theoretical calculation methods such as DFT and MD can reveal the essence of reactions at the atomic/electronic scale.[43] In the study of electrochemical degradation of PFAS, these methods can reveal the interaction between PFAS and electrodes as well as reaction energy barriers, and clarify the degradation mechanism. They can also predict the electronic structure and catalytic activity of electrode materials, thereby enabling the targeted design of high-efficiency catalysts.[44] In recent years, theoretical calculations have become an important tool in the research on the electrochemical degradation of PFAS.[45]

DFT calculations play an irreplaceable role in revealing the C–F bond cleavage mechanism, reaction energy barriers, and reaction pathway prediction of PFAS.[46] By constructing electrode-pollutant composite models, DFT can accurately simulate the adsorption configurations and adsorption energies of PFAS on the electrode surface, map the reaction potential energy surface, and gradually resolve the reaction energy barriers while identifying the rate-determining step.[42,47]

For instance, by calculating the C–F bond dissociation energy (BDE), Souza *et al.* pointed out that in PFOA, the α-C–F bond adjacent to the carboxyl group is more prone to cleavage due to the inductive effect.[48] In contrast, PFOS exhibits reduced reactivity of its distal C–F bonds owing to the electronic effect of the sulfonic group, which provides a theoretical basis for targeted degradation strategies.[48] Bentel *et al.* revealed the difference of C–F bond stability of different PFAS from the perspective of bond energy through DFT calculations, and showed the configuration and interaction of PFAS combined with electrons from the perspective of spatial structure, which together provided theoretical calculation evidence for the chemical behavior of PFAS under the action of electrons (Fig. 2a and b).[49] Zenobio *et al.* calculated the interaction between propylene and different PFAS using DFT, and confirmed that the interaction between propylene and PFOS and PFBS was more stable and the chemical activity of the formed system was lower, while the interaction activity with PFOA was relatively higher (Fig. 2c).[44]

In terms of reaction kinetics, Biswas *et al.* employed a DFT-based elementary kinetic approach to simulate the e_aq^- mediated defluorination process. Their work revealed that the average free energy barriers of PFOA and PFOS are 2.70 kJ mol^{-1} and 8.16 kJ mol^{-1}, respectively. This demonstrates that PFOS has lower reactivity due to a more compact solvation shell of solvated electrons, and for the first time, identifies that this process is governed by statistical kinetics rather than pure thermodynamics.[50] Blotevogel *et al.*, on the other hand, developed kinetic models for the reduction of PFAS by Fe^0/Zn^0 *via* DFT, noting that the electron transfer step is the RDS of defluorination.[51] In the context of material design, Mohamed *et al.* compared the adsorption energies of various PFAS on Fe^0 surfaces using DFT, finding that functional groups exert a greater influence on adsorption than carbon chain length.[52] The study by Wang *et al.* demonstrated that a higher Ti^{3+} content in Ti_4O_7 anodes can enhance the adsorption of PFOS and reduce electron transfer energy barriers. Meanwhile, only pores with a diameter larger than 1.03 μm exhibit electrochemical activity.[53,54] Ma *et al.*, by combining computational and experimental approaches, confirmed that MXene modification can strengthen electrostatic and hydrogen-bonding interactions between polyamide membranes and short-chain PFAS, achieving a synergistic improvement in selectivity and permeability.[55] Furthermore, Zhang *et al.* uncovered *via* DFT that the PFOA degradation pathway proceeds sequentially through two steps: reduction by photogenerated electrons to form $C_7F_{15}^{\cdot}$ radicals, followed by reaction with superoxide radicals to generate short-chain products. This work clarified the critical roles of electrons and superoxide radicals.[56] Raghavan *et al.* also observed that PFOA radicals undergo spontaneous decarboxylation in a vacuum environment, while the aqueous solvation effect inhibits this process. Applying

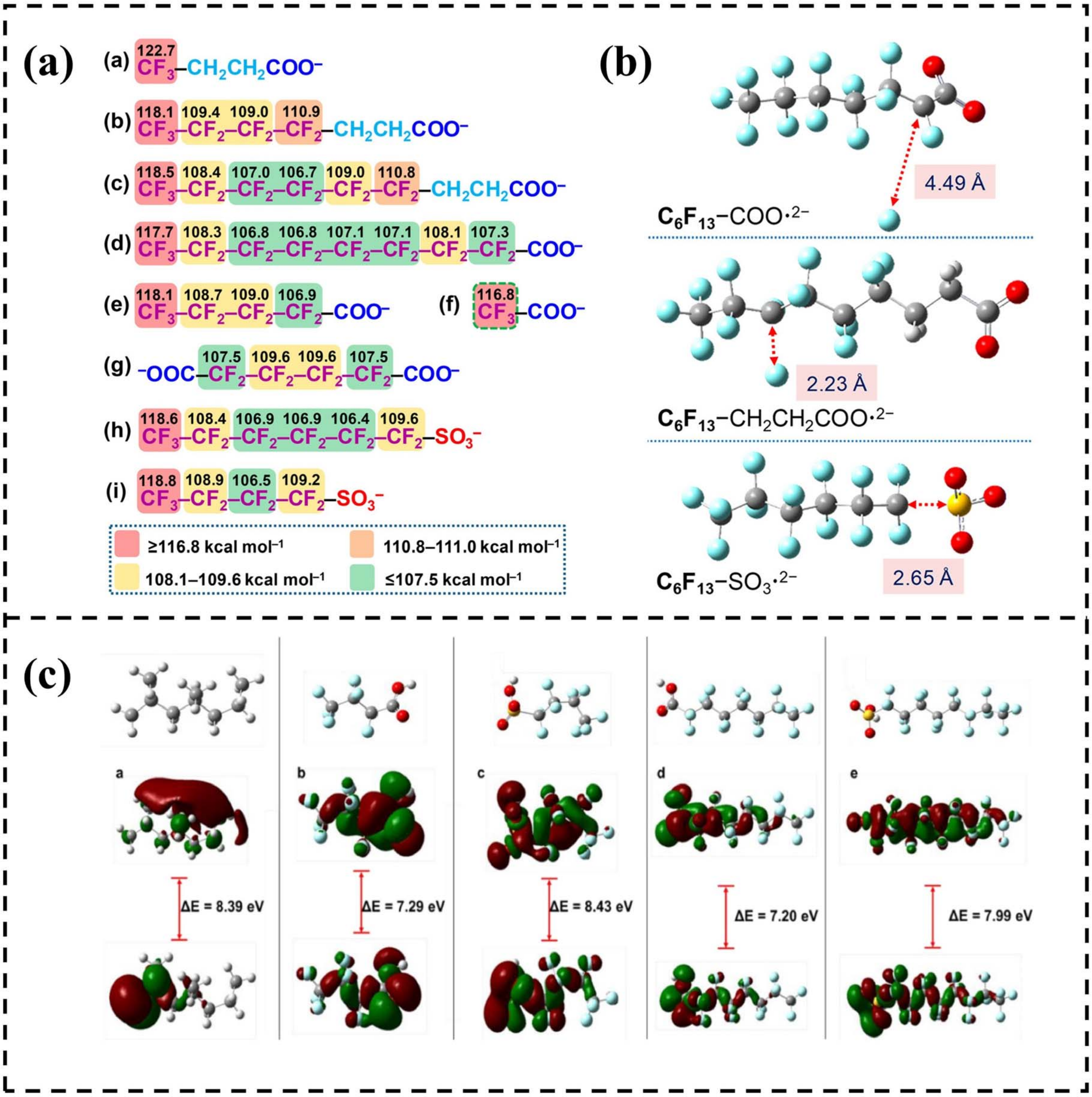

Fig. 2 (a) Calculation of C–F BDEs. (b) Structure of the adducts. Reproduced with permission.[49] Copyright 2019, American Chemical Society. (c) Frontier orbital distributions. Reproduced with permission.[44] Copyright 2022, Elsevier.

a potential of 3.08 V *vs.* the standard hydrogen electrode (SHE) reduces the decarboxylation activation energy by 0.34 eV and the reaction energy by 1.05 eV, with decarboxylation occurring before defluorination.[57] DFT calculations have revealed the polarization effect of the interfacial electrostatic field on PFAS molecules: a strong electric field alters the dipole moment orientation of PFOA molecules, leading to polarization and stretching of the carbon chain, which reduces the C–F bond energy by up to 40%. Specifically, for the α-CF_2 group, the energy barrier for nucleophilic attack by $O_2{\cdot}^-$ decreases from 1.78 eV to 0.92 eV, providing a theoretical explanation for the high defluorination efficiency observed experimentally.[58] Collectively, these studies demonstrate the systematic application value of DFT, ranging from uncovering PFAS degradation mechanisms at the electronic scale to guiding the design of functional materials.[59]

MD simulations, by capturing the diffusion and mass transfer behaviors of PFAS at electrode interfaces, multi-component interactions, and material interfacial dynamics, reveal the adsorption mechanisms and time-dependent processes of PFAS at the mesoscopic scale.[60] MD simulations further clarify how to facilitate PFAS degradation through environmental regulation or material design, thereby overcoming the limitations of methods like DFT in terms of system-scale and dynamic spatial effects.[61]

By combining MD and DFT calculations, Wang *et al.* discovered three binding modes between octadecyltrimethylammonium bromide (OTAB) and perfluoro-3-methylundecanoic acid (PFMeUPA). Among these, the electrostatic and hydrophobic synergistic effect accounted for the highest proportion and exhibited the lowest binding energy, which was identified as the dominant adsorption mechanism

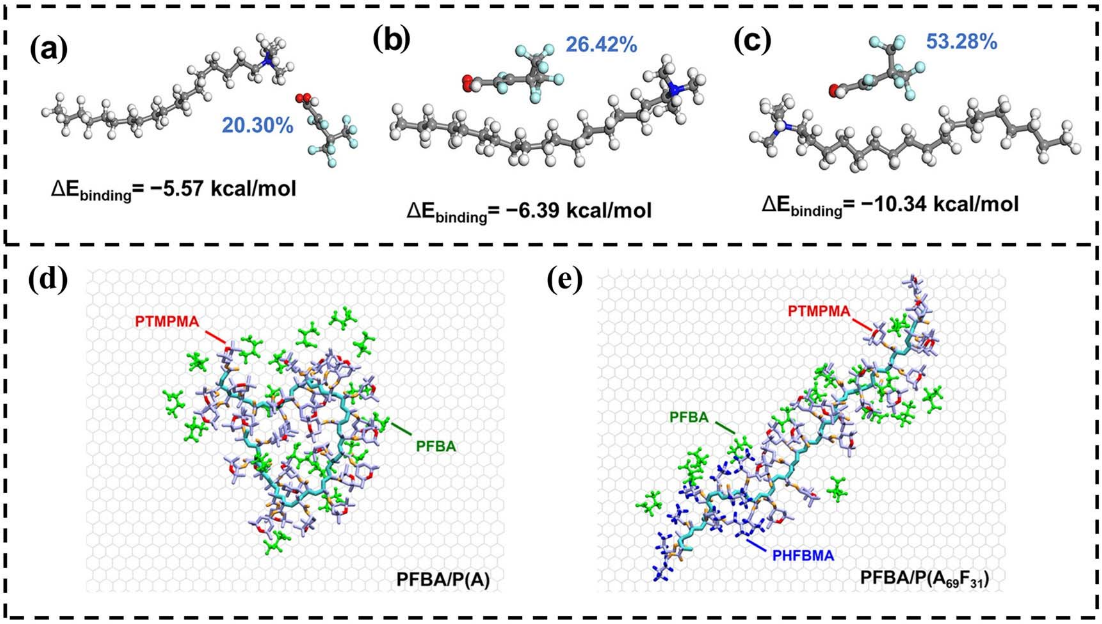

Fig. 3 (a–c) Three types of adsorption modes between OTAB and PFMeUPA.[53] Copyright 2023, American Chemical Society. Snapshots from copolymer MD simulations: (d) PFBA/P(A) and (e) PFBA/P($A_{69}F_{31}$). Reproduced with permission.[9] Copyright 2023, American Chemical Society.

(Fig. 3a–c).[53] Santiago *et al.* further validated this through MD simulations and electrosorption experiments, revealing that short-chain PFAS adsorb *via* both amino groups and fluorine-containing groups, with the strength of electrostatic interactions surpassing that of fluorophilic interactions.[9] As shown in Fig. 3d and e, when there is no fluorine group in the material, the groups containing amine will agglomerate, making it difficult for PFAS to contact the binding site. However, when the proportion of fluorine groups increases to 31%, this agglomeration is prevented, the material structure is looser, and PFAS can find the binding site more easily.[9]

From a thermodynamic perspective, the study by Willemsen *et al.* noted that PFAS adsorption is an entropy-driven process, and the entropy increase rises linearly with the number of CF_2 segments. This indicates that the hydrophobic effect makes a significant contribution to the adsorption of long-chain PFAS.[62]

Additionally, atomic-scale MD simulations by Lamb *et al.* demonstrated that the pH of the solution exerts a strong influence on the aggregation and adsorption behaviors of PFAS. Under neutral conditions, the headgroups of PFAS undergo deprotonation, and electrostatic repulsion leads to the formation of micelle-analogous assemblies that impede adsorption. In contrast, at acidic pH, the headgroups become protonated, electrostatic repulsion is reduced, and PFAS are more susceptible to be fully adsorbed on the graphene surface in a stacked manner.[63] Collectively, these studies establish a systematic understanding spanning molecular dynamic behaviors, interfacial interaction mechanisms, and external condition regulation-highlighting the crucial role of MD simulations in elucidating the environmental behaviors of PFAS.[64]

Theoretical calculations, leveraging the synergy and complementarity of DFT and MD, have emerged as pivotal tools for unraveling electrochemical PFAS degradation mechanisms and guiding rational technology design. DFT can resolve reaction pathways and activation barriers at the electronic scale, whereas MD captures dynamic interfacial behaviors and mass–transfer processes across broader spatiotemporal scales. Their integration bridges electron-transfer events with macroscopic kinetics, moving PFAS remediation from trial and error experimentation toward mechanism informed optimization.[44] Importantly, these theory tools also provide a direct data foundation for AI-enabled HTS: automated DFT/MD workflows can generate standardized descriptors and labels, such as PFAS adsorption energies on candidate electrode surfaces, key C–F bond cleavage and electron transfer barriers, interfacial solvation/ion-pairing characteristics, and stability relevant energetics, which are difficult to measure comprehensively in experiments.[65] When combined with high-throughput experimental outputs, such theory-derived features enable machine-learning models to learn structure activity relationships, prioritize promising materials and operating windows, and iteratively refine predictions through experimental validation.[10]

3 AI enabled high throughput screening for PFAS degradation

The exploration of electrode and catalyst remains a central bottleneck for electrochemical PFAS destruction because performance is jointly governed by PFAS adsorption at electrified interfaces, kinetic barriers of key steps, reactive-species generation, suppression of side reactions, and long-term stability in realistic matrices.[66] As a result, conventional one by one material optimization is often inefficient and provides limited guidance for PFAS destruction.[67] AI-enabled HTS offers an alternative by integrating large-scale experimental and theory derived datasets with machine learning to identify and validate high potential candidates in an iterative, closed loop manner.[68]

In a PFAS oriented workflow, AI-enabled HTS starts from generating mechanism relevant data at scale and then uses models to guide the next experimental or computational steps.[69] High throughput experiments can rapidly test material libraries and operating windows using standardized electrochemical protocols, while analytics such as LC-MS/MS and fluoride quantification provide performance labels beyond PFAS removal, including defluorination, current efficiency, and durability.[70] In parallel, automated DFT/MD can supply descriptors that are difficult to obtain comprehensively from experiments, such as adsorption energies of representative PFAS on candidate surfaces, as well as energetics associated with electron transfer and C–F bond activation.[71] Combining these experimental labels with theory derived descriptors enables supervised models to learn quantitative structure activity relationships and to prioritize candidates for validation.[72]

Fig. 4 illustrates the key idea of integrating intelligent proposal with rapid feedback. It contrasts the traditional search paradigm with a combined approach that uses a large language model and an evolutionary strategy to propose and refine candidate materials, followed by rapid preparation and high-throughput electrochemical testing.[73–76] In a PFAS context, the same pipeline can be used to propose candidate anode/cathode compositions or surface modifications, then quickly test them under standardized PFAS degradation protocols, and iteratively improve the candidate list based on measured removal, defluorination, and stability.[77]

For example, when predicting the adsorption energy of PFOA on candidate electrode surfaces,[78] a training set can be constructed based on DFT calculated adsorption energies across representative surfaces,[79] defect states,[80,81] and terminations,[82–86] alongside concise material descriptors that capture compositional and surface electronic properties.[87] The resulting model can screen large candidate pools and output a ranked shortlist of materials predicted to exhibit strong PFAS affinity.[88] This shortlist can then be refined through targeted calculations and validated *via* electrochemical degradation experiments.[89] Beyond single property predictions, the development of PFAS electrodes is intrinsically multi-objective.[90–92] For EO anodes, a high OEP is required to suppress parasitic oxygen evolution and broaden the usable oxidation window, while adequate PFAS affinity promotes interfacial electron transfer and maintains a reactive near-surface zone.[93,94] Therefore, model guided multi-objective screening aims to identify optimal tradeoffs rather than a single best solution.[95–97]

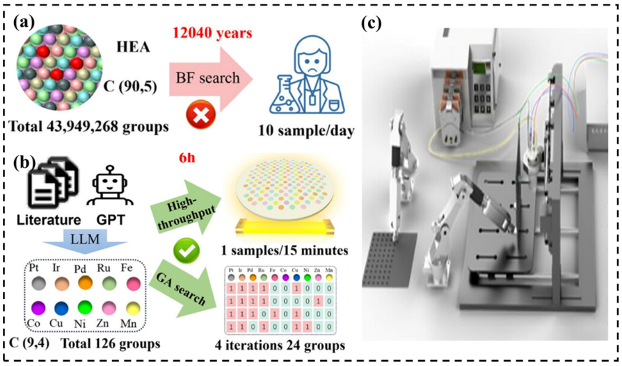

Pt	Ir	Pd	Ru	Fe	Co	Cu	Ni	Zn	Mn
1	1	1	1	0	0	1	0	0	0
1	1	1	1	0	0	0	0	1	0
1	1	1	0	1	0	1	0	0	0
1	1	0	1	0	0	1	1	0	0

Fig. 4 (a) The traditional search method. (b) The Combined method using LLM and genetic algorithm. (c) Schematic diagram of high-throughput electrochemical testing. Reproduced with permission.[76] Copyright 2025, Wiley-VCH GmbH.

To enable multi-objective optimization in PFAS electrochemistry, AI-enabled HTS is typically built as a workflow that combines descriptor construction, predictive modeling, and candidate generation.[98] Feature engineering remains essential because it translates intrinsic material properties into descriptors that are directly relevant to PFAS destruction, such as PFAS adsorption strength, OEP related characteristics for EO anodes, energetics associated with electron transfer and C–F activation, and stability proxies.[99–102] Depending on the research objective, different Machine Learning (ML) models can be deployed for prediction, screening, and design.[103] For example, supervised learning models trained on curated "composition/structure performance" datasets are frequently used to rapidly predict the performance of untested candidates.[104]

Fig. 5 highlights the complementary roles of different AI tools in this workflow. Domain adapted language models can support literature triage and structured extraction of PFAS relevant conditions and outcomes (Fig. 5a),[69,105] while graph based learning can capture structure property relationships to predict adsorption-related descriptors and redox–relevant properties (Fig. 5b).[70,106] In addition, generative models can propose new candidates under explicit performance constraints.[107]

Large Language Model (LLM) driven research frameworks can further assist knowledge base construction and experimental planning.[93] Although some demonstrations have been developed for other electrocatalytic reactions, they illustrate a transferable literature to experiment pipeline that can be adapted to PFAS electrochemistry for accelerating information retrieval, suggesting plausible parameter ranges (Fig. 5c).[76,108]

The key advantage of AI-enabled HTS is its closed loop iteration.[109] Through continuous feedback among experiments, computation, and modeling, the screening strategy and model accuracy can be progressively improved.[110] In a typical cycle, an initial dataset is used to train a model that proposes high potential candidates. These candidates are then prioritized for high-throughput testing and higher fidelity calculations, and the resulting validation data are added back to update the model.[111] Repeating this prediction validation update loop accelerates convergence toward materials that meet target performance criteria.[112]

Although challenges persist in terms of data, models, and practical applications, with the continuous advancement of AI technologies, the growing accumulation of data resources, and the deepening of interdisciplinary collaboration, AI-enabled HTS technology is expected to accelerate the development of PFAS remediation materials and provide more effective solutions for water resource protection and environmental pollution control.

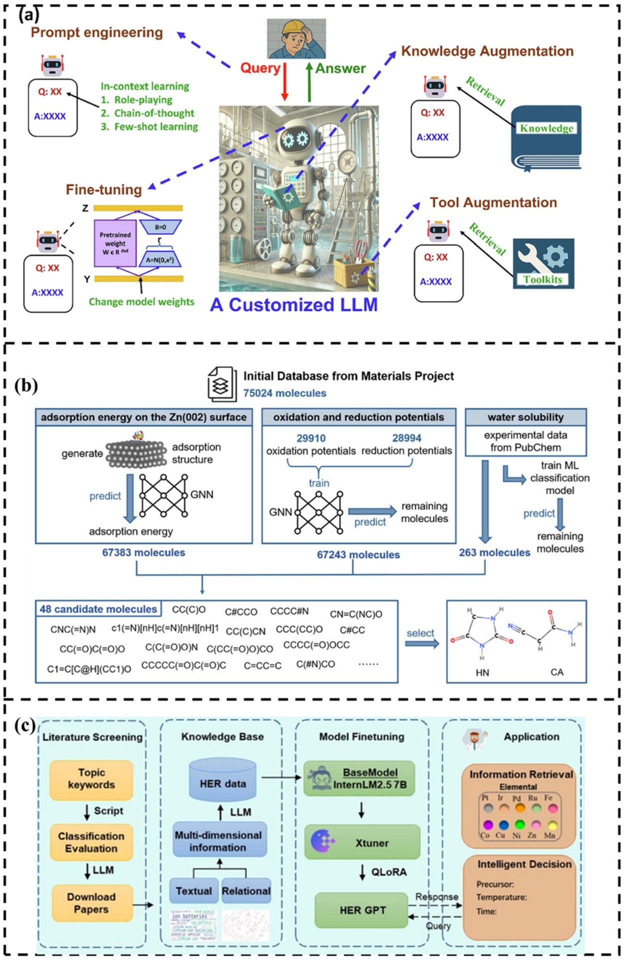

Fig. 5 (a) Three methods to adapt LLMs for wastewater management. Reproduced with permission.[69] Copyright 2025, Springer Nature. (b) The research workflow for HTS of high-performance electrolyte additive molecules. Reproduced with permission.[70] Copyright 2025, Wiley-VCH GmbH. (c) LLMs-driven research framework for HER materials. Reproduced with permission.[76] Copyright 2025, Wiley-VCH GmbH.

4 Electrochemical oxidation method for PFAS degradation

Electrochemical oxidation (EO) is an advanced oxidation technology that directly or indirectly degrades pollutants through electrochemical driving.[113,114] By applying an external electric field, it drives direct or indirect oxidation reactions of target pollutants at the anode interface, thereby achieving their degradation and mineralization. EO demonstrates distinct advantages for the removal of PFAS, which are characterized by exceptionally strong C–F bonds.[115] The efficacy of this technology hinges critically on the selection of anode materials and the oxidation processes induced under high applied potentials. On one hand, specific anode materials can generate highly reactive, surface-adsorbed ·OH or other potent oxidizing species, depending on the electrolyte composition at their surfaces.[116] On the other hand, anodes possessing high oxygen evolution overpotentials may facilitate the oxidation of PFAS molecules adsorbed onto their surface through a DET mechanism.[117] These robust oxidation pathways effectively attack and cleave the exceptionally stable C–F bonds within PFAS molecules, resulting in their stepwise defluorination and ultimate mineralization into harmless or low-toxicity inorganic end products, such as CO_2 and F^- ions.[118] The efficiency and reaction pathways of anodic oxidation are profoundly dependent on key factors, including the catalytic activity and stability of the electrode material, the composition of the electrolyte, and operational parameters.[65] A deep understanding of the mechanisms underlying these influencing factors and their interactions is fundamental for optimizing EO processes, enhancing PFAS removal efficiency, and improving energy utilization. This section will systematically explore the core mechanisms, electrode materials, and key influencing factors in the latest research advancements regarding PFAS degradation *via* EO.

4.1 EO degradation mechanism of PFAS

The core mechanisms for degrading PFAS *via* EO include direct oxidation and indirect oxidation.[119] These two pathways can operate independently or coexist synergistically, depending on the characteristics of electrode materials, electrolyte composition, and operating conditions. Direct oxidation relies on the specific adsorption of PFAS on the anode surface, where DET between the electrode and the adsorbed pollutants cleaves the C–F bonds. Indirect oxidation depends on strong oxidizing species generated at the anode, such as ·OH and $SO_4^{\bullet-}$. These radicals diffuse into the bulk solution to attack PFAS molecules non-selectively, with efficiency determined by the radical yield and lifetime.[120]

The hydrophobic perfluorinated chains of PFAS easily bind to the hydrophobic regions of electrodes through electrostatic interactions, van der Waals forces, hydrogen bonds, *etc.*, enhancing adsorption stability and optimizing electron transfer pathways.[116] Huang *et al.* revealed that in the amorphous Pd/Ti_4O_7 system, π conjugation further increased the adsorption energy from −22.3 kJ mol^{-1} to −38.6 kJ mol^{-1}. EPR and free radical probe experiments confirmed that almost no free radicals, like ·OH, were generated during the degradation process, indicating that the degradation mainly occurred through direct anodic oxidation. Therefore, the increase in adsorption energy directly affects the efficiency of electron transfer.[39]

The adsorption energy of PFAS with electrodes is crucial, and the high OEP of electrode materials is also key. Only when the applied anode potential exceeds the redox potential of PFAS, DET will occur, which effectively overlaps between the highest occupied molecular orbital (HOMO) of PFAS and the conduction band level of the electrode with high oxygen evolution potential, thus forming a direct electron transfer channel. Electrons are transferred directly from the adsorbed PFAS molecule to the anode.[41] Schaefer *et al.* verified that when the potential exceeds the oxidation potential of PFOS, adding the strong ·OH scavenger tert-butanol has little effect on the degradation rate of PFOS. This is completely consistent with the DFT-predicted DET pathway that "does not require ·OH mediation".[121]

Wang *et al.* elaborated on the mechanism of electrochemical degradation of PFOA using a Ti^{3+}/TiO_2-NTA anode (Fig. 6). Due to the pK_a value of PFOA being approximately 0, under the electrolysis experimental conditions, PFOA molecules are almost completely ionized into $C_7F_{15}COO^-$.[39] This anion loses an electron through DET on the anode surface, generating an unstable $C_7F_{15}COO^{\bullet}$ radical, marking the initiation of the degradation process (eqn (1)). Notably, Ti^{3+} self-doping significantly enhances the electrical conductivity of TiO_2 nanotubes, while Ti–F bonds formed on the anode surface promote the DET reaction through coulombic forces.[122] The generated $C_7F_{15}COO^{\bullet}$ radical immediately undergoes a Kolbe decarboxylation reaction, producing a $C_7F_{15}^{\bullet}$ radical and CO_2 (eqn (2)). This perfluoroalkyl radical ($C_7F_{15}^{\bullet}$) is attacked by ·OH generated near the anode, forming thermodynamically unstable $C_7F_{15}OH$ (eqn (3)). Subsequently, $C_7F_{15}OH$ undergoes intramolecular rearrangement (eqn (4)) and hydrolysis (eqn (5)), breaking a CF_2 unit and releasing HF. Through repeated "unzipping" cycles, PFOA is ultimately mineralized into CO_2 and HF. The experiment detected six short-chain PFCAs as intermediates, whose concentrations first increased and then decreased, confirming they serve as degradable intermediates. After 90 minutes of electrolysis, the system achieved remarkable mineralization: the total organic carbon (TOC) removal rate reached 93.3%, the defluorination rate was 74.8%, and an average of 12.8 F^- ions were released per degraded PFOA molecule.[122] These data strongly demonstrate that the electrochemical system efficiently converts PFOA into inorganic end products.

$$C_7F_{15}COO^- \rightarrow C_7F_{15}CO\dot{O} + e^- \tag{1}$$

$$C_7F_{15}COO^{\bullet} \rightarrow C_7F_{15}^{\bullet} + CO_2 \tag{2}$$

$$C_7F_{15}^{\bullet} + {}^{\bullet}OH \rightarrow C_7F_{15}OH \tag{3}$$

$$C_7F_{15}OH \rightarrow C_6F_{13}COF + H^+ + F^- \tag{4}$$

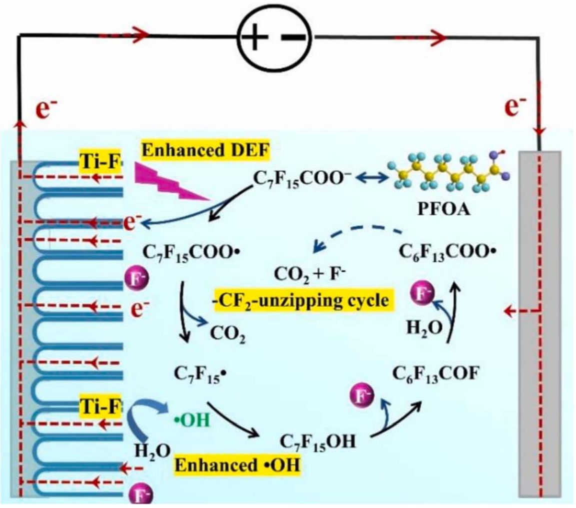

Fig. 6 Proposed degradation pathways of PFOA by electrochemical oxidation. Reproduced with permission.[122] Copyright 2021, Elsevier.

$$C_6F_{13}COF + H_2O \rightarrow C_6F_{13}COO^- + 2H^+ + F^- \tag{5}$$

Through experimental and theoretical calculations, Song *et al.* confirmed that under NaCl-containing conditions, Cl· is the key initial step triggering the degradation reaction of PFOA rather than DET.[42] The core mechanism involves the synergistic action between Cl· and ·OH. Experimental results demonstrate that under these conditions, PFOA degradation efficiency reached 89.4–94.9% within 480 minutes, with a corresponding defluorination rate of 38.7–44.1%. The specific degradation pathway is illustrated in Fig. 7a. Gibbs free energy (ΔG) calculations revealed that the ΔG for the Cl·-initiated reaction was 65.57 kJ mol^{-1}, significantly lower than that for the ·OH-initiated reaction (162.65 kJ mol^{-1}). Consequently, the first step of PFOA degradation is predominantly triggered by Cl·, generating the intermediate $C_7F_{15}COO\cdot$ (eqn (6)). In contrast, the same reaction without radical involvement exhibited a prohibitively high ΔG of 693.34 kJ mol^{-1}, unequivocally demonstrating that radicals are essential for effective PFOA degradation (Table 1). The resulting $C_7F_{15}COO\cdot$ subsequently undergoes decarboxylation. This step exhibits an extremely low activation energy barrier ($\Delta G^{\ddagger}$) of only 1.72 kJ mol^{-1}, facilitating rapid carboxyl group removal from the long-chain PFOA to yield the perfluoroalkyl radical $\cdot C_7F_{15}$, thereby initiating the carbon chain cleavage process. The $\cdot C_7F_{15}$ radical, synergistically with ·OH, progressively undergoes chain-shortening, defluorination, and hydrolysis reactions, ultimately forming short-chain PFCAs

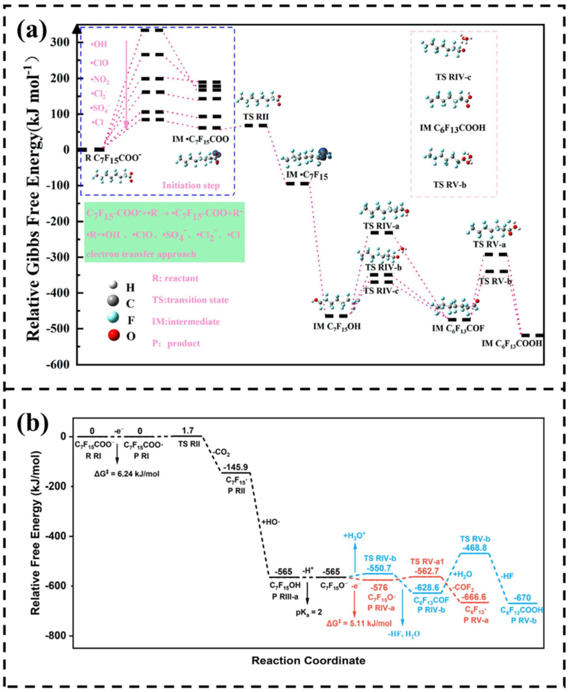

Fig. 7 (a) Scheme of the potential energy surface for the degradation of PFOA. Reproduced with permission.[42] Copyright 2023, American Chemical Society. (b) Profile of the potential energy surfaces for the electro-oxidation of $C_7F_{15}COO^-$. Reproduced with permission.[123] Copyright 2022, American Chemical Society.

Table 1 Possible reaction pathways for the degradation of PFOA with their ΔG and $\Delta G^{\ddagger}$ at the M06-2X/6-311++G(2d,2p) level of theory using SMD as the solvation model[42]

The possible reaction	ΔG (kJ mol^{-1})	$\Delta G^{\ddagger}$ (kJ mol^{-1})
$C_7F_{15}COO^- \rightarrow C_7F_{15}COO^{\bullet}$	693.34	
$C_7F_{15}COO^- + Cl^{\bullet} \rightarrow C_7F_{15}COO^{\bullet} + Cl^-$	65.57	80.93
$C_7F_{15}COO^- + \cdot OH \rightarrow C_7F_{15}COO^{\bullet} + OH^-$	162.65	330.16
$C_7F_{15}COO^{\bullet} \rightarrow C_7F_{15}^{\bullet} + CO_2$	−141.28	1.72
$C_7F_{15}^{\bullet} + {}^{\bullet}OH \rightarrow C_7F_{15}OH$	−412.92	No barrier
$C_7F_{15}OH + 2H_2O \rightarrow C_6F_{13}COF + HF + 2H_2O$	20.81	55.92
$C_6F_{13}COF + 2H_2O \rightarrow C_6F_{13}COOH + HF + H_2O$	−39.08	114.29

intermediates and further mineralizing. In summary, within this mechanism, Cl· primarily facilitates the low-energy-barrier initial activation, while ·OH governs the subsequent low-energy-barrier reactions involving chain cleavage, defluorination, and hydrolysis. The complementary functions of these two radicals collectively enable the highly efficient mineralization degradation of PFOA. This study provides a novel theoretical foundation and insights for utilizing electrochemical technologies to remove PFAS from the environment.[42]

$$C_7F_{15}COO^- + Cl^{\bullet} \rightarrow C_7F_{15}COO^{\bullet} + Cl^- \tag{6}$$

$$S_2O_8^{2-} \xrightarrow{BDD} 2SO_4^{\bullet -} \tag{7}$$

$$S_2O_8^{2-} + \cdot OH \rightarrow SO_4^{\bullet -} + HSO_4^- + 0.5O_2 \tag{8}$$

Chen *et al.*, through DFT simulations and experimental verification, proposed that the electrochemical degradation of PFOA is dominated by a direct oxidation pathway driven by holes. It achieves rapid mineralization through the "decarboxylation–hydroxylation–carbon chain cleavage" cycle and does not produce the short-chain PFCAs recognized traditionally.[123] Fig. 7b presents the reaction free energy change profile. The black parts represent the steps shared by the major and minor pathways, the red part represents the major pathway, and the blue part represents the minor pathway. In the major pathway, the $\Delta G^{\ddagger}$ of each step is extremely low (6.24, 1.7, 5.11, 13.3 kJ mol^{-1}), and the ΔG continuously decreases, with the reaction proceeding rapidly and spontaneously: during decarboxylation, ΔG drops sharply by − 145.9 kJ mol^{-1}, highlighting its core triggering role; in the alkyl radical hydroxylation stage, ΔG drops directly from − 145.9 to − 565 kJ mol^{-1}, with no obvious energy barrier and completion in an instant. In contrast, in the hydrolysis minor pathway, the transition states (such as TS RIV-b, TS RV-b) have high energy and large $\Delta G^{\ddagger}$, the reaction is slow, and only a small amount of short-chain PFCAs are generated. Overall, it verifies the degradation mechanism that "hole oxidation is the core driving force, ·OH assists, and hydrolysis is secondary", and clearly presents the thermodynamic and kinetic differences as well as the primary–secondary relationships of different pathways.

Zhao *et al.* innovatively proposed the electrochemical activation mechanism of persulfate (PS) in the BDD/PS system for the degradation of PFAS.[124] The electrooxidation of PFAS initiates from DET on the surface of BDD. Subsequently, under the action of reactive oxygen species (ROS), structural units of PFAS are gradually removed, shortening the carbon chain, and ultimately mineralizing into CO_2, H_2O, and F^- (Fig. 8a). On one hand, PS can be directly activated to generate $SO_4^{\bullet -}$ (eqn (7)). On the other hand, ·OH produced by the electrolysis of water can also react with PS to form $SO_4^{\bullet -}$ (eqn (8)). Compared with ·OH, $SO_4^{\bullet -}$ has a longer half-life and can efficiently degrade PFAS within a wide pH range (2–8). Meanwhile, its strong electrophilicity makes it more suitable for attacking the hydrophobic perfluorocarbon chains of PFAS. In addition, the BDD anode can promote the conversion of PS into a highly reactive transition state PS* through discharge, enabling the degradation of PFAS *via* a non-radical pathway. After activation by the BDD anode, PS destroys the C–F bonds of PFAS with great force through a synergistic action mode of radical and non-radical pathways. Pierpaoli *et al.* also explained the electrochemical oxidation reaction pathways of PFOA and PFOS, and the results are shown in Fig. 8b. PFOA undergoes direct electron transfer to generate radicals, followed by decarboxylation, and then undergoes gradual chain scission and defluorination upon interaction with oxygen or hydroxyl radicals. PFOS undergoes defluorination first, and then the sulfonic acid group decomposes, and the carbon chain is gradually shortened through reactions with water and hydroxyl radicals. Eventually, both are converted into inorganic products such as CO_2, HF, and SO_4^{2-}.[125]

In direct oxidation, PFAS molecules adsorb onto the electrode surface and undergo DET. This process aids in breaking the C–F bonds, but it requires overcoming significant adsorption free energy barriers and high electrode potentials. In contrast, indirect oxidation achieves the deep mineralization of PFAS through non-selective radical attacks. However, it still faces challenges in effectively cleaving C–F bonds. Given the strength of C–F bonds, direct and indirect oxidation often act in concert. Taking the BDD electrode as an example, it efficiently degrades the adsorbed PFAS *via* the DET mechanism on its surface, while the ·OH radicals generated at the anode oxidize the pollutants in the solution phase. This synergistic mechanism of direct and indirect oxidation enhances the overall degradation efficiency by up to 40% compared to single-action pathways.[114] Future research should focus on the kinetics of C–F bond cleavage, the interfacial electron transfer mechanism in synergistic systems, and the transformation pathways of highly stable intermediate products.

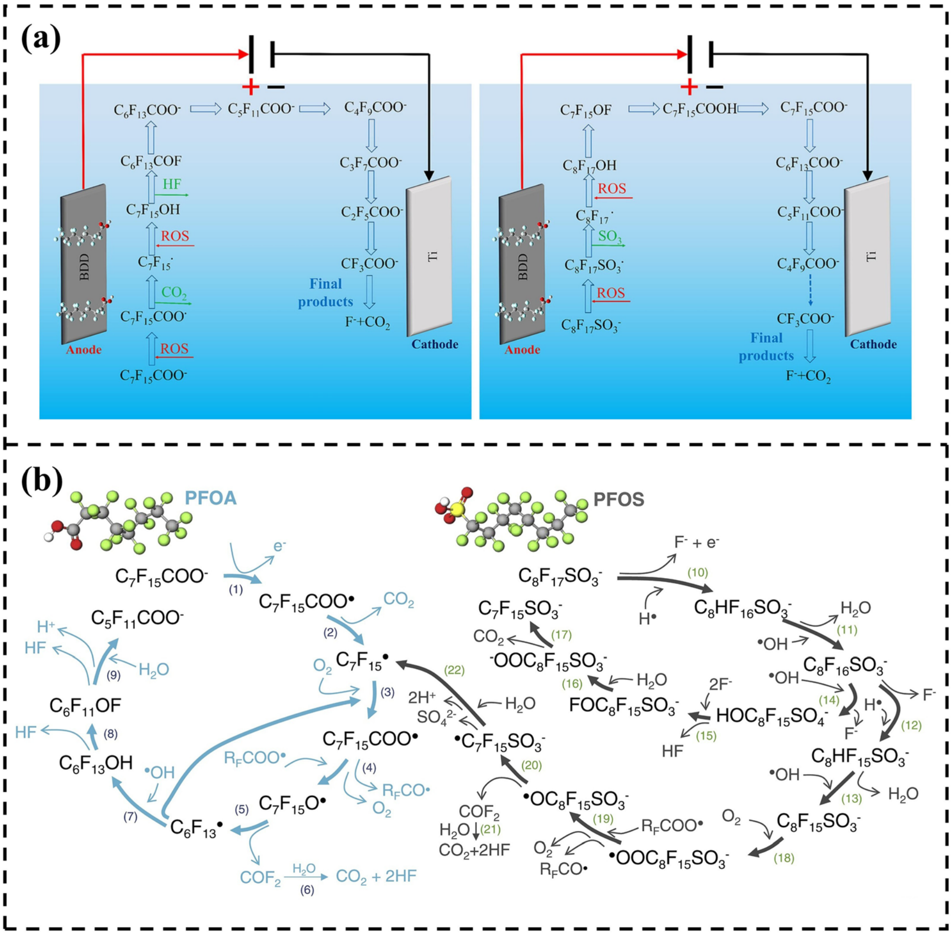

Fig. 8 (a) Proposed degradation pathway of PFOA and PFOS in the BDD/PS system. Reproduced with permission.[124] Copyright 2024, Elsevier. (b) The possible reaction pathway for the PFOA and PFOS. Reproduced with permission.[125] Copyright 2020, Elsevier.

4.2 Investigation of parameters in EO for PFAS degradation

4.2.1 Electrode materials. In the research on EO for PFAS degradation, the properties of anode materials are critical factors determining degradation efficiency and reaction pathways.[126] From the perspective of electrochemical degradation of PFAS, electrode microstructure and surface chemistry should be designed to address three intrinsic challenges: interfacial preconcentration, mass-transfer limitation at trace concentrations, and the trade-off between strong affinity and surface deactivation. PFAS molecules are amphiphilic and often exist as anions in water, which makes their interfacial enrichment highly sensitive to surface charge, hydrophobic, and local electric fields. At environmentally relevant ng–μg L^{-1} levels, anodic oxidation frequently becomes transport-limited. Therefore, 3D porous or flow-through architectures can improve PFAS flux to reactive sites and increase oxidant utilization. Meanwhile, adsorption must be sufficiently strong to facilitate direct electron transfer or sustain near-surface radical chemistry, but not so strong that intermediates poison the surface. These PFAS-guided principles provide a mechanistic basis for interpreting why doping, composite construction, and hierarchical porosity often enhance EO performance, and they should be considered alongside OEP and stability when comparing anode materials.

Core parameters of different anode materials, such as electron transfer capacity, distribution of catalytic active sites, ·OH generation efficiency, OEP, interfacial reaction kinetics, and chemical stability, directly regulate the mineralization efficiency of PFAS and the distribution of intermediate products. An ideal anode material must simultaneously satisfy the following requirements: a high OEP to suppress competitive oxygen evolution reactions, excellent chemical stability to adapt to long-term operation in complex electrolyte environments, and optimized surface properties to enhance PFAS adsorption affinity and reduce electron transfer impedance. For these reasons, materials such as BDD,[127] Magnéli phase Ti_4O_7, PbO_2, and SnO_2 have become the focus of current research. A systematic analysis of their performance differences (the comparison of PFAS removal efficiencies shown in Table 2), action mechanisms, and application potential is of key significance for advancing the development of EO technologies.[128]

BDD electrodes demonstrate significant advantages in PFAS treatment due to their wide potential window, high OEP, and unique dual degradation mechanism combining DET with synergistic indirect ·OH oxidation.[121] The BDD anode itself has

Table 2 PFAS removal efficiency and other conditions of commonly used anode materials in EO systems in recent years[a]

PFAS	Initial concentration	Anode material	Cathode material	Electrolyte	pH	Current density (mA cm^{-2})	Applied potential (V)	PFAS removal (%)	Ref.
PFOA	1 mg L^{-1}	BDD	Ti	Na_2SO_4 + NaCl	3–7	40	25	94	33
PFOS								89.1	
PFHxS								88.1	
PFOA	50 μM	BDD	Ti	PS	3.8	40		99.9	124
PFOS									
PFOS	100 mg L^{-1}	BDD/SnO_2–F	Pt	NaCl	3	30		95.6	129
PFOA		BND	Pt	Na_2SO_4	4.8	4	2.5 V *vs.* SCE	99.3	130
PFOA	20 mg L^{-1}	BDD	Stainless steel	Na_2SO_4	7	10		97.9	131
PFBA								65.6	
GenX								84.9	
6:2 FTCA								99.4	
GenX	0.25 mmol L^{-1}	BDD	Gr–Ni–foam	K_2SO_4	3	16		92.2	132
PFOA	0.1 mg L^{-1}	BDD	Stainless steel	K_2HPO_4 + H_3PO_4	7	25		89	125
PFOS								84	
PFOA	1350 ng L^{-1}	BDD	Stainless steel		7.8	75		80	125
PFOS	3280 ng L^{-1}							78	
PFOA	0.1 mg L^{-1}	BDD	Stainless steel	K_2HPO_4 + H_3PO_4	7	75		99.9	125
PFOS								84	
PFOA	100 mg L^{-1}	Ti/SnO_2–Sb	Ti	$NaClO_4$	5	10	9	90.3	133
PFOA	100 mg L^{-1}	Ti/SnO_2–Sb/PbO_2	Ti	$NaClO_4$	5	10	9	91.1	133
PFOA	100 mg L^{-1}	Ti/SnO_2Sb/MnO_2	Ti	$NaClO_4$	5	10	9	31.7	133
PFOS	20 μmol L^{-1}	$(Ti_{1-x}Ce_x)_4O_7$	Stainless steel	Na_2SO_4		20	2.5	98.9	31
PFOS	20 μmol L^{-1}	Ti_4O_7	Stainless steel	Na_2SO_4		20	2.5	86.2	31
PFOS	0.0929 mmol L^{-1}	Ti/TiO_2-NTs/Ag_2O/PbO_2	Ti	$NaClO_4$		30		74.87	134
PFBS								5.39	
PFHxS								15.43	
PFOS	0.0929 mmol L^{-1}	Ti/PbO_2	Ti	$NaClO_4$		30		41.59	134
PFOS	0.0929 mmol L^{-1}	Ti/TiO_2–NTs/PbO_2	Ti	$NaClO_4$		30		50.87	134
PFOS	0.2 μM	BRGO sponge	Spontex	Na_2HPO_4/NaH_2PO_4	7.2	230	7.6 V *vs.* SHE	67	37
PFOA								48.9	
PFBA								16.6	
PFBS								38.6	
PFHxS								49.1	
PFHxA								32.8	
PFOA	0.5 mM	Ti_4O_7	Stainless steel	$NaClO_4$		5	3.9	99.9	135
PFOA	0.5 mM	Ce–PbO_2	Stainless steel	$NaClO_4$		5	3.5	99.5	135
PFOA	0.5 mM	BDD	Stainless steel	$NaClO_4$		5	3.8	98.8	135
PFOS	0.1 mM	Ti_4O_7	Stainless steel	$NaClO_4$		5	3.9	93.1	135
PFBA	100 mg L^{-1}	Ce–PbO_2	Ti	$NaClO_4$		20		31.8	136
PFPeA								41.4	
PFHxA								78.2	
PFHpA								97.9	
PFOA								96.7	

Table 2 (*Contd.*)

PFAS	Initial concentration	Anode material	Cathode material	Electrolyte	pH	Current density (mA cm^{-2})	Applied potential (V)	PFAS removal (%)	Ref.
PFOA	2.0 μM	Ti_4O_7	Stainless steel	Na_2SO_4	7	5	3.322 V *vs.* SHE	>90	47
PFOS									
PFOA	4.14 mg L^{-1}	Ti_4O_7 REM	Stainless steel	K_2HPO_4			3.3 V *vs.* SHE	99.9	137
PFOS	5 mg L^{-1}	Ti_4O_7 REM	Stainless steel	K_2HPO_4	7		3.6 V *vs.* SHE	99.9	137
PFOA	50 mg L^{-1}	Ti^{3+}/TiO_2-NTA	Ti	Na_2SO_4	3–11	2		98.1	122
PFOA	50 mg L^{-1}	Ti/SnO_2–Sb–Bi	Ti	$NaClO_4$	4.7	22	3.37 V *vs.* SCE	99	138
PFNA	0.25 mmol L^{-1}	Ti/SnO_2–Sb–Ce	Ti	$NaClO_4$	3	10		95.8	34
PFDA								88.7	
PFNA	0.25 mmol L^{-1}	Ti/SnO_2–Sb/Ce–PbO_2	Ti	$NaClO_4$	3	10		97.1	34
PFDA								92.2	
PFNA	0.25 mmol L^{-1}	Ti/BDD	Ti	$NaClO_4$	3	10		98.7	34
PFDA								96	
GenX	10 mg L^{-1}	N-GS/CeO_2@Ti_4O_7	Stainless steel	$NaClO_4$		20	3.55	97	139
GenX	10 mg L^{-1}	Ti_4O_7	Stainless steel	$NaClO_4$		20	3.55	86.8	139
GenX	10 mg L^{-1}	Ti/RuO_2–Ir_7	Stainless steel	$NaClO_4$		20	3.55	50	139
PFOS	2.0 μM	Ti_4O_7 REM	Stainless steel	Na_2SO_4		40	1.6–3.5 V *vs.* SHE	90	54
PFOA	20 ppm	Ti_4O_7 REM	Carbon felt	Na_2SO_4		28.6	14	92	140
PFOS	50 mg L^{-1}	3DG-PbO_2	Stainless steel	Na_2SO_4	7	30		96.2	38
PFOA	0.12 mM	Ti_4O_7/Pd	Ti	Na_2SO_4	7.2	10	6	86.7	39
PFUnA	0.093 ng L^{-1}	Ti–ZnO	Stainless steel	None	7.23	20		46.43	141
PFDA	0.055 ng L^{-1}							53.25	
PFNA	0.046 ng L^{-1}							45.45	
PFOA	5.43 ng L^{-1}							65.84	
PFHpA	3.52 ng L^{-1}							58.03	
PFHxA	2.77 ng L^{-1}							49.31	
PFPeA	2.73 ng L^{-1}							44.79	
PFBA	2.95 ng L^{-1}							40.74	
PFOS	4.74 ng L^{-1}							63.42	
PFHxS	3.64 ng L^{-1}							39.66	
PFBS	0.86 ng L^{-1}							38.95	
PFOA	100 mg L^{-1}	Ti/SnO_2–Sb_2O_5/PbO_2-PVDF	Ti	$NaClO_4$	3	40	5–15	92.1	142
PFOS	100 mg L^{-1}	Ti/Sn–Sb/SnO_2 –F–Sb	Ti	$NaClO_4$	3	20		99.6	36
PFOA	100 μmol L^{-1}	Ti	CNTs-graphene		3.6		0.6	96.9	143
PFOS								97	
6:2 FTS	20 mg L^{-1}	Ti/SnO_2–Sb_2O_5–Bi_2O_3		$NaClO_4$	6.94	6.8	5	26.8	144
PFOS								5.5	

[a] Perfluorooctanoic acid (PFOA); perfluorooctane sulfonate (PFOS); perfluorohexane sulfonate (PFHxS); perfluorobutanoic Acid (PFBA); hexafluoropropylene oxide dimer Acid (GenX); 6:2 fluorotelomer carboxylic acid (6:2 FTCA); perfluorobutane sulfonate (PFBS); perfluorohexane sulfonate (PFHxS); perfluorohexanoic acid (PFHxA); perfluoropentanoic acid (PFPeA); perfluoroheptanoic acid (PFHpA); perfluorononanoic acid (PFNA); perfluorodecanoic acid (PFDA); perfluoroundecanoic Acid (PFUnA); 6:2 fluorotelomersulfonic acid (6:2 FTS).

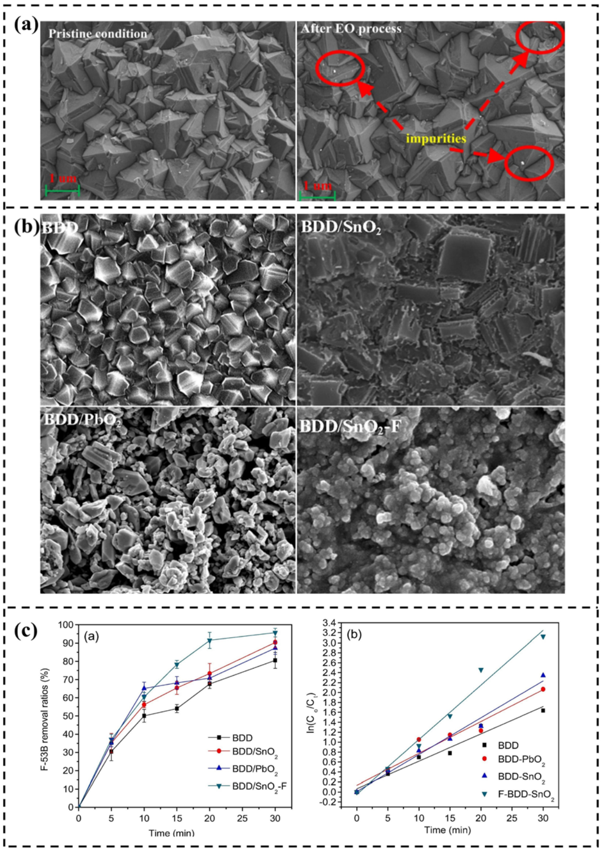

Fig. 9 (a) SEM of BDD. Reproduced with permission.[124] Copyright 2024, Elsevier. (b) SEM images of BDD, BDD/SnO_2, BDD/PbO_2, and BDD/SnO_2–F, respectively. (c) Degradation ratios and the first-order kinetics analysis. Reproduced with permission.[129] Copyright 2019, Elsevier.

high chemical stability and is not easily corroded. As shown in Fig. 9a, Zhao *et al.* compared the surface structure of the BDD anode in its original state with that after the EO process, clearly demonstrating the performance advantages of the BDD anode.[124] Zhuo *et al.* prepared four kinds of electrodes, BDD, BDD/SnO_2, BDD/PbO_2 and BDD/SnO_2–F, and their morphologies are shown in Fig. 9b respectively.[129] Among them, BDD/SnO_2-F has finer and dispersed surface particles due to the introduction of fluorine. This change in morphology and material is crucial to the degradation performance. Through finer dispersed particles, it increases the specific surface area and OEP, and can more efficiently adsorb and degrade 6:2 chlorinated polyfluoroether sulfonate (F-53B), so that its degradation rate of F–53B can reach 95.6% in 30 minutes, which is much better than other electrodes (Fig. 9c).[129] Olvera-Vargas *et al.* confirmed through DFT calculations that GenX requires overcoming an energy barrier of 3.2 eV ($E° = 3.65$ V *vs.* SHE) for oxidation in acidic media. The upper limit of the BDD electrode's potential window (approximately 3.0 V *vs.* SHE) is significantly higher than that of Pt (1.9 V *vs.* SHE), thermodynamically satisfying the conditions for DET reactions.[132] Simultaneously, at high potentials, BDD generates surface-adsorbed ·OH *via* the water discharge reaction, effectively enhancing indirect oxidation while suppressing electrode poisoning caused by intermediate product adsorption. This dual mechanism, "DET-initiated C–F bond cleavage followed by surface ·OH-mediated deep mineralization," is key to its efficient PFAS degradation. Optimizing the electrode's microstructure is crucial for enhancing BDD degradation efficiency.[145] Saleh *et al.* found that the degradation rate of PFBA-C4 was only 14% after 6 hours using a planar BDD electrode, whereas a mesh-plate composite electrode ((M + P)-BDD) achieved 97% degradation within 4 hours at 20 mA cm^{-2}. This disparity stems from the three-dimensional mesh structure of (M + P)-BDD, which increases the specific surface area to promote greater ·OH generation through water ionization while reducing surface resistance, significantly optimizing reaction kinetics. For degrading PFHxA-C6, the removal rate achievable with P-BDD at 20–25 V was attained by (M + P)-BDD at only 6–8 V, effectively reducing voltage loss and energy consumption. This indicates that electrode structural design can fully unlock the application potential of BDD in PFAS degradation.[146]

Compared with the costly BDD anode, titanium suboxide (TSO) has significant cost advantages (approximately \$0.36/m^2), a high OEP (>2.5 V *vs.* SHE), good electrical conductivity (~1000 S cm^{-1}), and excellent chemical stability. It is regarded as a powerful alternative to traditional anodes such as BDD in the field of EO degradation of PFAS. Moreover, the preparation process of TSO anodes usually avoids the use of toxic dopants like Sb and Pb, further reducing environmental risks.[29,47] Under neutral pH conditions, the degradation selectivity of TSO for PFAS is generally higher than that of BDD electrodes, which helps reduce the oxygen evolution reaction (OER) side reaction. Theoretical calculations by Wang *et al.* showed that the energy barrier for C–S bond cleavage of PFOS on Ti_4O_7 is lower than that on Ti_9O_{17}. Experiments have confirmed that, benefiting from the higher Ti^{3+} content and optimized pore size, Ti_4O_7 anodes have more advantages in PFOS degradation efficiency and energy efficiency (Fig. 10a).[54] A study by Gomri *et al.* using a Ti_4O_7-based reactive electrochemical membrane (REM) anode showed that increasing the current density and feed concentration, and reducing the REM flux can effectively improve the PFOA removal rate.[140] Le *et al.* used an energy-saving Magnéli phase Ti_4O_7-REM anode to treat PFOA and PFOS, which not only achieved a high removal rate but also had an low energy consumption. The high specific surface area and flow-through operation of this technology significantly enhanced mass transfer and reaction rates.[137]

The high overall porosity and interconnected porous network structure of Ti_4O_7 electrodes significantly promote mass transfer of PFAS and increase the reaction area. Combined with its large electroactive surface area and low local current density, high electrolysis efficiency can be achieved. The macroporous Magnéli phase Ti_4O_7 ceramic anode prepared by Lin *et al.* has an electroactive surface area 1302 times larger than its geometric area (Fig. 10b).[135] This anode, which combines a high OEP (2.7 V *vs.* SCE), significant ·OH generation capacity, and DET capability, exhibits a higher oxidation rate for PFOA/PFOS than Ce-doped PbO_2 and Ti/BDD electrodes(Fig. 10c).[135] Despite these significant advantages, Ti_4O_7 electrodes still face

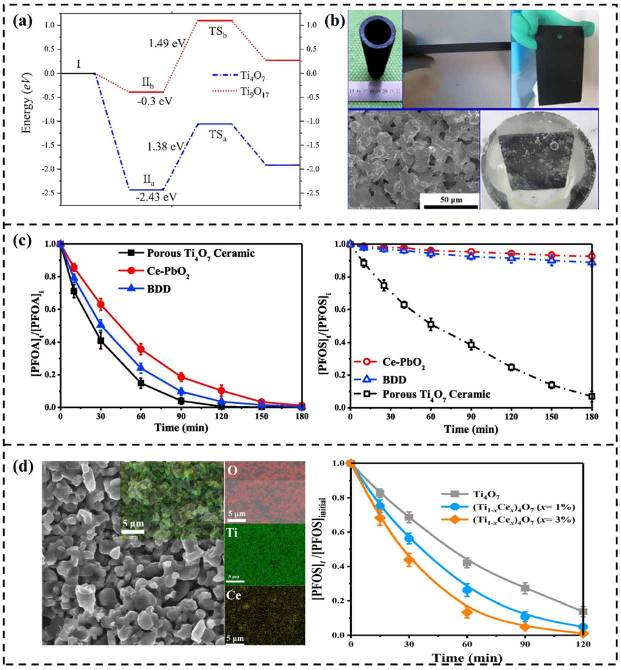

Fig. 10 (a) Energetics of PFOS with Ti_4O_7 and Ti_9O_{17} clusters.[54] Copyright 2021, Elsevier. (b) Ti_4O_7 ceramic materials. (c) Concentration changes during the electrooxidation process. Reproduced with permission.[135] Copyright 2018, Elsevier. (d) SEM image of the fabricated $(Ti1\text{-}xCex)_4O_7$ (x = 3%) electrode and corresponding EDX elemental mappings, and the concentration change of PFOS oxidation. Reproduced with permission.[31] Copyright 2021, American Chemical Society.

challenges such as low interfacial charge transfer rate and insufficient ·OH yield.[147] Ti_4O_7-based composite materials designed through heterostructure construction and defect engineering can further improve performance while maintaining stability and low-cost advantages. For example, Lin *et al.* introduced additional oxygen vacancies into Ti_4O_7 electrodes through Ce^{3+} doping, which optimized the electronic structure, reduced charge transfer resistance, promoted ·OH generation, and significantly enhanced electrocatalytic performance(Fig. 10d).[31] The amorphous Pd-loaded Ti_4O_7 electrode developed by Huang *et al.* achieved efficient direct anodic oxidation of PFOA by enhancing electron transfer and pollutant binding capacity, and the degradation process was less susceptible to quenching by common anions.[39]

In the field of EO for PFAS degradation, element doping, material compositing, and porous structure design have emerged as core strategies to enhance anode performance. These strategies significantly strengthen the electrode's ability to degrade PFAS by precisely regulating the material's electronic structure, interfacial properties, and microtopography.

Element doping improves the degradation efficiency of PFAS by modifying the electronic structure and surface abilities of electrode materials. Rare earth element doping exhibits significant effects. For instance, Niu *et al.* found that doping rare earth elements into titanium-based lead dioxide electrodes can effectively increase the density of surface defects and the content of reactive oxygen species, promote the activation of water molecules and the generation of ·OH, while enhancing the corrosion resistance and stability of the electrode, thus greatly improving the adsorption and oxidation efficiency of PFAS. The prepared Ce-doped porous nanocrystalline PbO_2 electrode showed superior performance in treatment capacity, degradation efficiency, and mineralization degree compared to the Ti/SnO_2–Sb electrode when treating C_4–C_8 PFCAs.[136] Non-metallic element doping is also effective. Liu *et al.* designed a B/N co-doped diamond (BND) electrode, which regulates the electronic structure through the synergistic effect of B and N.[130] In addition, the PVDF-doped modified PbO_2 electrode, by inhibiting grain growth and enhancing hydrophobicity, extended the electrode lifespan to 45.75 hours, and the PFOA degradation rate was improved to 92.1%.[142]

Composite electrodes achieve performance complementarity and synergistic enhancement by combining the characteristics of different materials. The combination of highly catalytically active metal oxides, such as MnO_2 and RuO_2, with conductive substrates like titanium mesh and graphite felt can synergistically promote the generation of ·OH while ensuring good conductivity and mechanical stability. The Ti^{3+} self-doped TiO_2 nanotube array (Ti^{3+}/TiO_2-NTA) anode prepared by Wang *et al.*, which combines self-doping with a nanotube structure, achieved a PFOA degradation rate of 98.1%, a TOC removal rate of 93.3%, a defluorination rate of 74.8%, and an energy consumption of only 7.6 Wh/L after 90 minutes of electrolysis at a current density of 2 mA cm^{-2}.[122] The Ti/SnO_2–Sb–Bi anode and Ti/TiO_2–NTs/Ag_2O/PbO_2 anode developed by Zhuo *et al.*, by integrating various materials and constructing multi-layered interface architectures, electron transfer and the generation of reactive oxygen species are further facilitated, allowing for the efficient degradation of PFOA, PFOS, and their alternative compounds.[134,138] The Ti/Sn–Sb/SnO_2–F–Sb electrode prepared by Yang *et al.*, through the co-doping of F and Sb combined with a Sn–Sb interlayer, extended the electrode lifespan from 80.1 h to 103.1 h, with a PFOS removal rate exceeding 99% within 120 minutes.[36]

Porous design enhances electrochemical reaction efficiency by increasing the specific surface area of electrodes and promoting mass transfer. The N-GS/CeO_2@Ti_4O_7 heterojunction composite membrane electrode prepared by Liang *et al.* utilizes the porous structure and the "cementing" effect of CeO_2 to achieve stable encapsulation of N-GS. Its high specific surface area (3.2 m^2 g^{-1}) and defect sites accelerate charge transfer, reducing the R_{ct} to 5 Ω. In the EO of GenX, the degradation efficiency reaches 97% within 120 minutes, and the defluorination rate reaches 70–90% when treating actual wastewater.[139] The three-dimensional (3D) graphene-lead dioxide (3DG-PbO_2) composite anode developed by Duan *et al.* optimizes the crystal size of PbO_2 through the 3D network structure of 3DG and enhances ·OH generation capacity. The degradation rate constant of PFOS by this anode is 2.33 times that of the pure PbO_2 anode.[38] In addition to such structural designs, porous electrodes composed of different material combinations also exhibit excellent performance.[34,133]

It is crucial to emphasize that high PFAS removal efficiency does not strictly equate to deep mineralization. Many modified anodes rapidly deplete parent PFAS molecules but yield low defluorination ratios, indicating the accumulation of recalcitrant short-chain intermediates. This discrepancy highlights the necessity of matching the electrode's microstructural design with the unique physicochemical properties of PFAS. Since PFAS are amphiphilic molecules with highly stable perfluorinated tails, optimizing the interfacial wettability of the electrode can forcibly drive these molecules into the Helmholtz layer, thereby enhancing DET. Furthermore, simply increasing the macroscopic surface area is insufficient. The rational design of hierarchical porous structures introduces a spatial confinement effect. These tailored microporous and mesoporous networks not only selectively enrich PFAS through hydrophobic interactions but also trap the generated ROS and intermediate short-chain fragments within the confined microenvironment. By significantly prolonging the residence time of intermediates near the active sites, this microstructural regulation effectively bridges the gap between superficial removal and ultimate defluorination.

4.2.2 Electrolyte. In the current research on the degradation of PFAS by EO, the electrolyte system significantly affects the degradation kinetics and mineralization depth by regulating the generation of active species, interfacial electric field, and mass transfer efficiency. It can be mainly divided into four categories: chlorine-containing electrolytes, sulfate electrolytes, inert electrolytes, and strong alkaline electrolytes, each with distinct mechanisms of action and efficacy.

The core role of chlorine-containing electrolytes (such as NaCl) is to enhance degradation by generating reactive chlorine species ($Cl\cdot$, $ClO\cdot$, HClO). Their oxidation potential ($Cl\cdot/Cl^-$: $E^\circ = 2.4$ V *vs.* SHE) is higher than that of $\cdot OH$ ($E^\circ = 2.0$ V), enabling efficient attack on C–F bonds. Meanwhile, Cl^- can react with $\cdot OH$ to form $ClOH^{\cdot-}$, which is then converted into $Cl\cdot$, further enhancing the oxidizing capacity.[129] However, their effectiveness is influenced by electrode materials. In the BDD electrode system, the presence of Cl^- has less than a 20% impact on the degradation efficiency of PFOA/PFOS, because the generated perchlorates and other substances have limited competition with the DET pathway.[121,133] Zhuo *et al.* found that on Ti/PbO_2 electrodes, an appropriate amount of Cl^- (<10 mM) increased the defluorination rate of F-53B from 72.9% to 77.4%, but high concentrations of Cl^- could cause passivation of the surface of electrodes such as PbO_2. However, a drawback of this system is the easy formation of toxic by-products like ClO_4^-, and when the Cl^- concentration exceeds 10 mM, the amount of ClO_4^- produced is positively correlated with the degradation efficiency of PFAS.[65]

Inert electrolytes (such as $NaNO_3$, $NaClO_4$), due to the lack of participation of active anions, rely only on DET and indirect oxidation by $\cdot OH$, so the degradation rate of PFAS is usually lower than that in systems containing active electrolytes.[130,131] Their advantage is that they can avoid the formation of toxic by-products like ClO_4^-, making them suitable for scenarios with high requirements for product purity.

Different from chlorine-containing electrolytes, the role of SO_4^{2-} in sulfate systems (represented by Na_2SO_4) is dual. On one hand, SO_4^{2-} may react with $\cdot OH$ to form $S_2O_8^{2-}$ with weaker oxidizing ability, resulting in a decrease in PFAS degradation efficiency.[129] On the other hand, SO_4^{2-} can be electrochemically activated to generate strongly oxidizing $SO_4^{\cdot-}$ ($E^\circ = 2.5$–3.1 V), and at this time, the degradation rate of PFOA is 2.3–3.4 times higher than that in systems with inert electrolytes ($NaNO_3$, $NaClO_4$).[130]

The core role of strong alkaline electrolytes (such as KOH, LiOH) is to enhance mass transfer by constructing a strong interfacial electric field. For example, high concentrations of OH^- can accumulate in the nanopores of the electrode, forming a strong interfacial electric field, which increases the mass

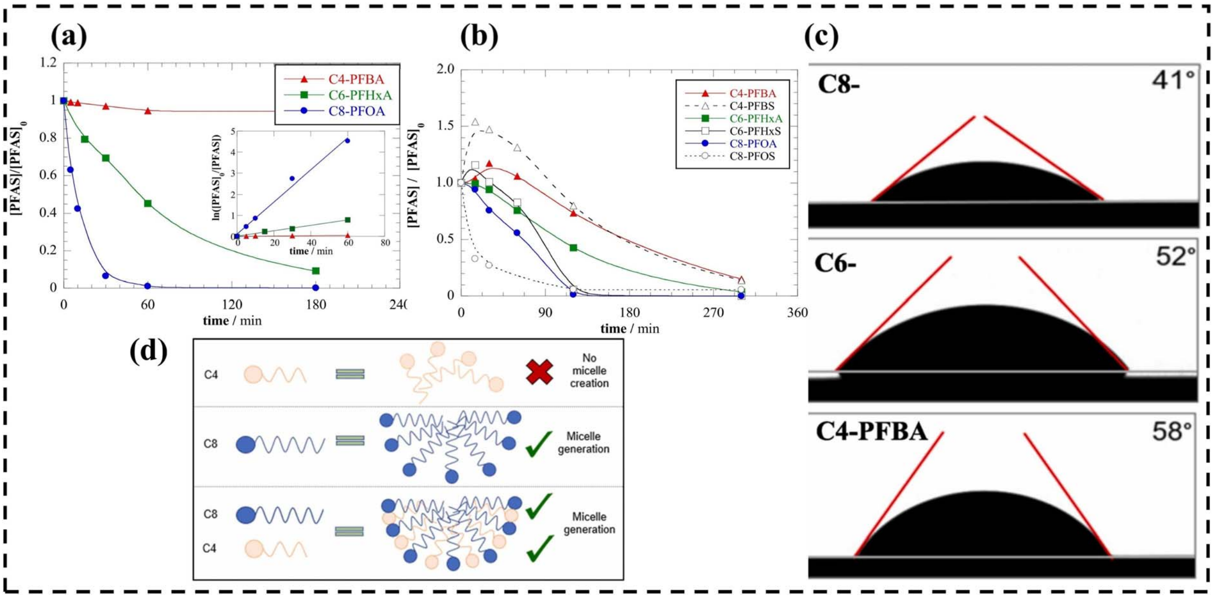

Fig. 11 (a) BDD electrodes for single-solute solutions of each PFCA. (b) Degradation effect of multi-solute model wastewater matrix. (c) Sessile drop surface contact angle. (d) Schematic of hetero-micelle formation. Reproduced with permission.[149] Copyright 2022, Elsevier.

transfer coefficient of PFAS to the anode from 0.01 cm s^{-1} to 0.03 cm s^{-1}.[122] Extreme alkaline conditions (such as 8.0 M LiOH) can also compensate for the potential gap through the electric field, achieving complete defluorination of PFOS.[148]

In summary, different electrolyte systems affect the efficiency of EO degradation through differentiated mechanisms, and their selection needs to be comprehensively considered in combination with degradation efficiency, by-product risks, and practical application scenarios.

4.2.3 The properties of PFAS.

The molecular structural characteristics of PFAS, such as carbon chain length and functional group type, as well as their existing forms, are the core intrinsic factors determining the efficiency of EO degradation.[47] In-depth analysis of the correlation between these properties and degradation efficiency has an important guiding value for the precise optimization design of EO technology.

Unlike their long-chain counterparts, short-chain PFAS lack a substantial hydrophobic tail, rendering conventional adsorption mechanisms driven by hydrophobic interactions highly inefficient. Consequently, these highly soluble molecules easily escape the anodic oxidation zone before deep mineralization can occur. Nienhauser *et al.* confirmed that the longer the carbon chain, the easier the degradation of PFAS (Fig. 11a), and that the long-chain PFAS will reduce the electrode contact angle (Fig. 11c).[149] However, in multi-component systems, the degradation of short-chain PFAS is significantly enhanced because they co-aggregate with long-chain homologues to form mixed micelles(Fig. 11b and d).[149]

To address this challenge, electrode materials designed specifically for short-chain PFAS removal should balance hydrophobicity and hydrophilicity to facilitate both adsorption and diffusion. For example, increasing the surface area and incorporating functional groups such as hydroxyl, carboxyl, or sulfonic acid groups can enhance the interaction with short-chain PFAS, facilitating their concentration at the electrode surface. Additionally, the use of porous carbon materials or conductive polymers with controlled pore sizes can improve the mass transfer of short-chain PFAS, providing better access to reactive sites and improving degradation efficiency. The development of electrode materials tailored for short-chain PFAS degradation should focus on enhancing the adsorption efficiency while maintaining high electrochemical activity for the efficient generation of reactive species, such as hydroxyl radicals or sulfate radicals, that are effective in breaking down these more water-soluble contaminants.[136]

Functional groups directly affect the difficulty of C–F bond cleavage through electronic effects and spatial configurations. For example, Wang *et al.* found that on TSO electrodes, the degradation rate of PFOS containing sulfonic acid groups ($-SO_3H$) is higher than that of PFOA with carboxylic acid groups ($-CO_2H$). The core mechanism lies in the fact that the high electronegativity of $-SO_3H$ can activate adjacent carbon atoms, which is more conducive to the addition reaction of ·OH free radicals.[47] Steric hindrance can inhibit degradation efficiency. GenX (C_6) containing $-CF_3$ branches has a significantly lower degradation rate (84.9%) than linear-structured PFOA (97.9%) because the branches hinder the contact between the $-CO_2H$ and the electrode surface. In contrast, 6:2 FTCA has a degradation rate of up to 99.4% due to the presence of C–H bonds in its molecule that are easily attacked by ·OH, showing the optimal performance.[131]

In multi-solute systems, the degradation rate of PFAS is generally higher than that in single-solute systems. This improvement is largely ascribed to the micellar structures formed by mixed PFAS on the electrode surface, which effectively reduces the electrode-solution contact angle. Consequently, the contact between short-chain PFAS and the electrode surface is significantly promoted, with their degradation rate increasing by up to 30% compared to that in single-solute systems.[149] Even in complex mixed systems containing multiple types of PFAS, although the degradation of PFOA (C_8) generates intermediates like PFBA(C_4), the overall degradation rate of the system remains higher than that of the corresponding single-solute systems.[149] In addition, the actual properties of polluted water sources have a significant impact on the electrochemical oxidation efficiency of PFAS. High electrolyte concentrations in actual industrial wastewater usually facilitate the generation of oxidants, thereby accelerating the degradation of PFAS, and their removal efficiency may even be higher than that in ultrapure water systems. However, when the water body contains excessively high concentrations of organic substances, these organics will compete with PFAS for active sites on the electrode surface or oxidants, thereby inhibiting the degradation efficiency of PFAS.[149]

In summary, the initial properties of PFAS regulate EO efficiency through multiple mechanisms. Long-chain PFAS enhance degradation kinetics by virtue of their high adsorption energy and the effect of improving interfacial wettability. The $-SO_3H$ group accelerates reactions by activating adjacent carbon atoms through its electronegativity. Mixed solute systems produce a synergistic effect through the formation of surface micelles. Considering the complex coexisting environment in actual water bodies, efficient removal of PFAS can be achieved by regulating extreme alkaline conditions or selecting specific electrolytes to strengthen the interfacial electric field or free radical pathways.

4.2.4 Electric current.

As a core external factor influencing the energy consumption of PFAS degradation by EO, the precise regulation of current properties has become a key approach to addressing bottlenecks including excessive energy requirement and the challenge of eliminating short-chain PFAS in this technology.[150] $*j*$ dominates degradation kinetics and efficiency by regulating the rate of free radical generation and mass transfer efficiency. In the low $*j*$ region (<10 mA cm^{-2}), the reaction is kinetically controlled and follows a pseudo-first-order model. In the high $*j*$ region (>30 mA cm^{-2}), the reaction shifts to mass transfer control and conforms to zero-order kinetics. When $*j* = 40$ mA cm^{-2}, the ·OH flux on the electrode surface tends to saturate, enabling efficient and simultaneous removal.[132,146] The synergistic optimization of system resistance can significantly improve electrical conductivity, allowing efficient PFAS removal even at relatively low $*j*$ while reducing energy consumption.[33]

Table 3 PFAS removal efficiency and other conditions of commonly used electrode materials in ER systems studied in recent years[a]

PFAS	Anode‖cathode	Electrolyte	pH	Reaction time (min)	Current density (mA cm^{-2})	Applied potential (V)	PFAS removal (%)	Ref.
PFOA (100 mg L^{-1})	BDD‖Fe_3O_4-rGA	Na_2SO_4	6	720	20	9.5	98.25	152
PFOA (100 mg L^{-1})	BDD‖Cu-rGA	Na_2SO_4	6	720	20	9.5	98.91	152
PFOA (100 mg L^{-1})	BDD‖rGA	Na_2SO_4	6	720	20	9.5	98.91	152
PFOA (100 mg L^{-1})	BDD‖graphite	Na_2SO_4	6	720	20	9.5	81.68	152
PFOA (100 mg L^{-1})	BDD‖Ti	Na_2SO_4	6	720	20	9.5	60.28	152
PFOA (36 mM)	TiO_2 mesh‖carbon paper molecular copper	MeCN + TBA ClO_4		240	5		93	40
PFOA (1 mM)	TiO_2 mesh‖Au	$KHCO_3$	9.5	840		−1.80 V *vs.* Ag/AgCl		41
PFMeUPA (100 μM)	Ti sheet‖GAC	Na_2SO_4		420		10	100	61
PFOS (100 μM)				240		15	10	
PFOA (10 mg L^{-1})	Pt‖Co–CN_2–Fe_2O_3 modified gas diffusion electrode	Na_2SO_4	2	120		−0.06 V *vs.* RHE	96.1	153
PFOS (5 ppm)	Pt‖CNT-CTAB	$NaClO_4$	11.5	120		−0.58 V *vs.* Ag/AgCl	92.2	35
PFOA (100 mg L^{-1})	Pt‖Rh/Ni	$Fe(C_5Me_5)_2$		1440		−1.25 V *vs.* Ag/AgCl	50.38	154
TFMAA (5 mg L^{-1})	Pt‖ZIF-67/C@CP	$Na_2HPO_4\cdot 12H_2O$ $NaH_2PO_4\cdot 2H_2O$		2880	-2.29×10^{-3}	−1.2 V *vs.* Ag/AgCl	99.66	155
TFMAA (5 mg L^{-1})	Pt‖CP	$Na_2HPO_4\cdot 12H_2O$ $NaH_2PO_4\cdot 2H_2O$		2880	-2.29×10^{-3}	−1.2 V *vs.* Ag/AgCl	18.98	155
TFMAA (5 mg L^{-1})	Pt‖C@CP	$Na_2HPO_4\cdot 12H_2O$ $NaH_2PO_4\cdot 2H_2O$		2880	-2.29×10^{-3}	−1.2 V *vs.* Ag/AgCl	92.31	155
PFMeUPA (5 mg L^{-1})	Pt‖MWCNT–COOH–OTAB	$Na_2HPO_4\cdot 12H_2O$ $NaH_2PO_4\cdot 2H_2O$	7		10.75	−1.6 V *vs.* Ag/AgCl	99.81	53
GenX (5 mg L^{-1})	BDD‖Cu	Na_2SO_4 NaCl		120	13.5		66	156
GenX (5 mg L^{-1})	BDD‖Ti	Na_2SO_4 NaCl		120	13.5		52	156
GenX (5 mg L^{-1})	BDD‖Au	Na_2SO_4 NaCl		120	13.5		92	156

[a] 2-(Trifluoromethyl)acrylic acid (TFMAA).

Compared with continuous electrolysis, pulsed electrolysis reconstructs the electrode microenvironment through periodic on–off cycles of current, which can promote the reorganization of the electrical double layer, renewal of the diffusion layer, and regeneration of ·OH, reduce electrode polarization, and thus show significant advantages. For example, the defluorination rate of PFOS can be increased to 1.5 times that of continuous electrolysis, achieving complete defluorination in only 60 pulse cycles, while energy consumption is significantly reduced by approximately 5.256 kWh m^3. This is mainly attributed to the inhibition of ineffective side reactions and the optimization of charge transfer efficiency.[148] Specific pulse parameters can further enhance degradation efficiency.

In summary, strategies such as precise regulation of *j*, adoption of pulsed electrolysis mode, and optimization of system resistance can synergistically improve PFAS degradation efficiency, promote deep removal of short-chain pollutants, and significantly reduce energy consumption. Future research should further explore the mechanisms by which different combinations of current properties affect the degradation of complex PFAS systems and promote the application and transformation of these optimization strategies in practical wastewater treatment engineering.

4.2.5 Other factors. pH value is a crucial regulatory parameter in the research on the degradation of PFAS by EO.[151] It determines the degradation efficiency and pathways by influencing the generation efficiency of ROS, the existing forms of PFAS, and the reaction processes on the electrode surface. Under acidic conditions, it is beneficial to the generation of $SO_4^{\bullet -}$ and inhibits the OER, thereby significantly improving the degradation rate. Meanwhile, PFAS mainly exists in protonated form, which enhances its interaction with the electrode surface, making it easier to trigger the key decarboxylation reaction and achieve efficient degradation. For example, a study by Zhuo *et al.* showed that the degradation rate of PFBS (C_4) can reach 92.1%.[142] However, a strongly acidic environment also increases the risk of electrode corrosion. In contrast, the high OH^- concentration under alkaline conditions can promote the generation of ·OH, and extremely alkaline conditions can even form a strong interfacial electric field, improving mass transfer efficiency.[122] But OH^- will competitively occupy the active sites of the electrode, inhibit the direct oxidation of PFAS, and significantly trigger OER, leading to increased energy consumption and decreased degradation efficiency.[142] The neutral pH condition faces the challenge that bicarbonate (HCO_3^-) and carbonate (CO_3^{2-}) ions can quench free radicals, resulting in reduced PFAS degradation efficiency.[113] To sum up, pH value mainly dominates the EO degradation process of PFAS by regulating the types and abundance of ROS, the ionization form of PFAS, and its adsorption behavior on the electrode surface. Therefore, in engineering practice and research, it is necessary to accurately optimize the pH value of the reaction system according to the specific characteristics of the target PFAS and treatment requirements to achieve efficient and stable degradation, providing a solid theoretical support and effective technical path for addressing PFAS pollution.

5 Electrochemical reduction method for PFAS degradation

As an emerging technology, electrochemical reduction (ER) can efficiently degrade C–F bonds in PFAS molecules through the dissociative electron transfer (DET) model or indirect reduction pathways, achieving deep defluorination and demonstrating low energy consumption potential. Compared with EO, ER has significant advantages in energy consumption control and defluorination selectivity, and is particularly suitable for the treatment of long-chain PFAS. Current research mainly focuses on overcoming key technical bottlenecks such as hydrogen evolution reaction (HER) competition, limitations of the electrochemical stability window of solvents, electrode surface passivation, secondary pollution, and low energy conversion efficiency. Optimization approaches include precise design of cathode materials, systematic analysis of reaction mechanisms, and scientific regulation of reaction conditions. The ER research on PFAS removal in recent years is shown in Table 3.

5.1 ER degradation mechanism of PFAS

In the ER of PFAS, the key difference between DET and indirect reduction lies in the electron transfer pathway and the dependence on catalysts.[157] DFT calculations indicate that efficient ER of PFAS requires two key conditions: the applied potential is lower than −2 V (*vs.* SHE), and the reaction transition state energy barrier is less than 40 kJ mol^{-1}.

When investigating the ER mechanism of PFOA, Calvillo-Solís *et al.* first revealed through reaction kinetics analysis that this reaction follows a concerted reaction mechanism—electron transfer and C–F bond cleavage occur simultaneously (electron transfer coefficient $\alpha < 0.5$), rather than a stepwise mechanism where electron transfer and bond cleavage proceed sequentially ($\alpha \geq 0.5$) (Fig. 12a). The realization of this concerted mechanism is closely related to the adsorption behavior of PFOA on the electrode surface: the potential energy curve in Fig. 12b shows that the adsorption of PFOA on the electrode surface can significantly reduce the reaction activation energy barrier, laying a thermodynamic foundation for the simultaneous occurrence of electron transfer and C–F bond cleavage. From the perspective of the specific reaction pathway on the gold electrode surface (Fig. 12c), PFOA first adsorbs on the inner Helmholtz plane of the electrode, then accepts electrons to undergo a reduction reaction, accompanied by C–F bond cleavage and defluorination; the generated intermediate species further interact with water or OH^- to complete the subsequent transformation.[41] Through theoretical analysis of frontier orbitals and electron density difference (Fig. 12d), the researchers revealed the orbital energy distribution of PFOA molecules, electron transfer sites, and the variation law of molecular electron density after electron injection from the perspective of electronic structure, which provides a key theoretical basis for clarifying the nature of electron transfer.[41] Furthermore, the results of free energy calculation (Fig. 12e) show that at a potential of $U = -2.84$ V s. SHE, the free energy from PFOA reactants, transition state (TS) to reduction

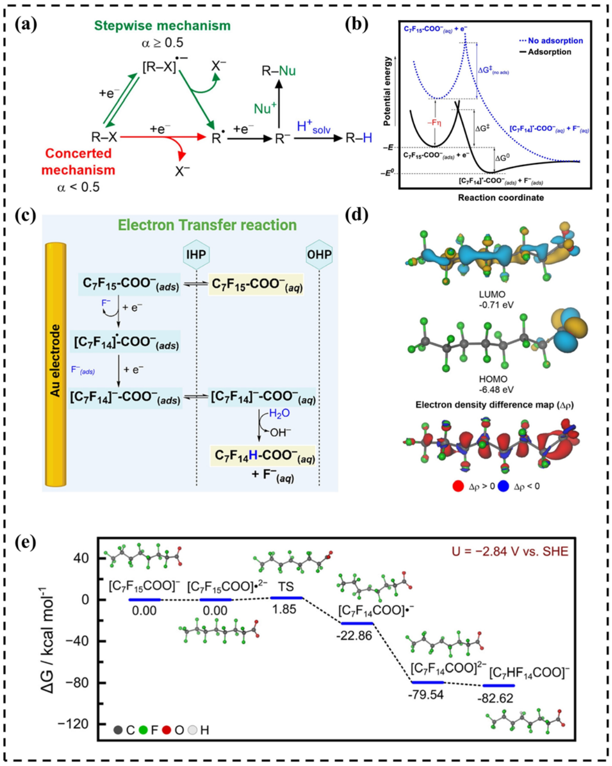

Fig. 12 (a) Two possible mechanisms. (b) Potential energy diagram. (c) Proposed degradation mechanism. (d) HOMO and LUMO orbitals and Electron density difference map. (e) Calculated Gibbs free energy potential energy surface. Reproduced with permission.[41] Copyright 2024, American Chemical Society.

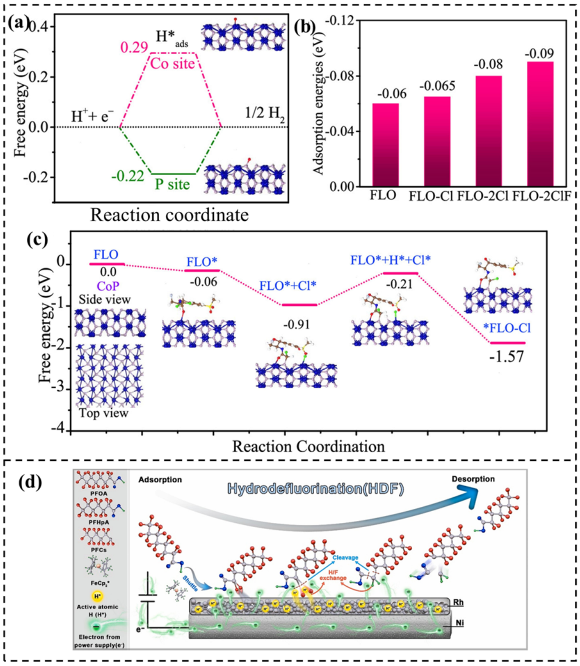

Fig. 13 (a) DFT-calculated free energy pathways. (b) Adsorption energies of FLO and intermediates. (c) Free energy diagram. Reproduced with permission.[160] Copyright 2019, American Chemical Society. (d) Proposed mechanisms for the HDF of PFOA on Rh/Ni cathode. Reproduced with permission.[154] Copyright 2021, Elsevier.

products, shows a gradual decreasing trend, which further verifies the feasibility of this concerted reduction pathway from a thermodynamic perspective.[158,159]

In addition, a study by Wang *et al.* first confirmed that C–F bond cleavage can be achieved through DET alone, and clarified that the C=C unsaturated structure in PFAS molecules is the key to promoting C–F bond cleavage because it is more likely to accept electrons, while saturated intermediates are difficult to further defluorinate, which provides a new basis for understanding the structure dependence of PFAS degradation.[53]

Indirect reduction exhibits stronger universality in PFAS degradation. It relies on the electrolysis of water on the electrode surface to generate $^{\bullet}$H and e_aq^-, which achieve defluorination through hydrogen–fluorine exchange and hydrogenation reactions, requiring catalyst stabilization.[49,160] Liu *et al. via* DFT calculations demonstrated that the P sites of crystalline cobalt phosphide (CoP) are more favorable for $^{\bullet}$H generation, providing key reactive species for dehalogenation (Fig. 13a). Fig. 13b shows that florfenicol (FLO) and its dehalogenated intermediates can stably adsorb on the CoP surface, and the higher the degree of dehalogenation, the stronger the adsorption, ensuring the continuous progress of the reaction. Fig. 13c presents that the free energy reaction pathway of FLO dechlorination on CoP is thermodynamically spontaneous throughout, and each step is easy to occur.[160] Together, these three aspects reveal the intrinsic mechanism of CoP efficiently catalyzing FLO dehalogenation.[155]

In the process of decomposing PFOA by ER using a Rh/Ni cathode, Zhu *et al.* verified that the core of the indirect reduction mechanism is hydrodefluorination (HDF). This mechanism does not involve the direct transfer of electrons to PFOA molecules; instead, it relies on active atomic hydrogen (H) generated *in situ* at the cathode as a reducing agent to indirectly mediate the cleavage and substitution of C–F bonds in PFOA (Fig. 13d). The H stored in the Rh lattice nucleophilically attacks the adsorbed PFOA molecules, gradually replacing the F atoms therein. Under the attack of H, the C–F bonds break, F^- ions detach, and C–H bonds are formed. This stepwise defluorination process is driven by the electrons continuously supplied by the cathode to maintain the reaction momentum, ultimately promoting the gradual degradation of PFOA into short-chain fluorinated intermediates and F^- ions.[154]

Tan *et al.* from Westlake University found that the mechanism dominated by e_aq^- is the core pathway for the current cathodic reduction of PFAS. As the strongest reducing agent, e_aq^- (E^0 = −2.87 V *vs.* SHE) can efficiently break C–F bonds. Further clarification using Marcus' theory and DET calculations shows that the activation free energy of electron transfer (ET) is much higher than that of the defluorination step, confirming that ET is the rate-limiting step rather than the direct cleavage of C–F bonds. The activation free energy of ET depends on the molecular structure of PFAS. For example, the CF_2COO^- group and the long-chain region are more likely to accept electrons, while ether bonds or short chains will hinder electron transfer.[161]

Both DET and H pathways have also been confirmed to participate in the reaction synergistically. Grunfeld *et al.* found that the activated carbon cathode can directly transfer electrons to PFAS through surface functional groups at a potential of −1.4 V *vs.* SHE, while atomic hydrogen generated by hydrolysis assists in defluorination.[61]

The catalytic synergistic mechanism is enhanced through the surface modification of electrode materials, with the core being the regulation of reaction pathways by introducing catalytically active sites. For example, the molecular copper electrocatalyst designed by Sinha *et al.* can achieve a 93% degradation rate and 99% defluorination rate of PFOA through 4-hours cathodic controlled current electrolysis at room temperature, with a current-normalized pseudo-first-order rate constant as high as 3.32 L h^{-1} A^{-1}, which is far superior to traditional high-temperature, high-pressure, or high-energy-consuming processes.[40] The nickel catalyst designed by Doi *et al.* can drive the multi-step C–F bond cleavage of perfluoroalkyl aromatics under mild conditions of 60 °C without extreme reaction environments.[162] The cobalt complex designed by Liu *et al.* can target the cleavage of low-bond-energy tertiary C–F bonds in branched PFAS, achieving 16/19 C–F bond cleavage.[163] Different metal active centers exhibit varying effects on PFAS reduction. Therefore, it is necessary to further screen metals with high activity, such as exploring new transition metals or their combinations. By altering the oxidation state and ligand environment of metals, their adsorption and activation capabilities for C–F bonds in PFAS can be adjusted to enhance catalytic efficiency and selectivity. In addition, the catalytic performance can be optimized by controlling the morphology, particle size, and pore structure of the catalyst. Preparing nano-sized catalysts increases the specific surface area and the number of active sites; designing porous structures facilitates the diffusion and mass transfer of PFAS molecules, thereby improving reaction efficiency. Furthermore, constructing composite catalysts by combining materials with different functions, leveraging their respective advantages, enables efficient and selective reduction of PFAS.

5.2 Investigation of parameters in ER for PFAS degradation

5.2.1 Electrode materials. The selection of cathode materials plays an important role in the efficiency of the ER of PFAS. The physicochemical properties of PFAS impose additional microstructure requirements because many target PFAS are anionic and experience electrostatic repulsion near negatively polarized cathodes. Effective ER therefore benefits from interfacial preconcentration strategies that combine hydrophobic interactions with cationic/ion-pairing motifs, enabling PFAS to access electron-rich sites. Porous conductive networks can further increase the density of reactive interfaces and tune local environments that control the generation and lifetime of key reducing species, while catalyst site design should balance selective C–F activation against competing HER.

Carbon-based materials have garnered significant attention owing to their low cost and scalability for practical applications. Activated carbon, one of the most commonly used cathode materials, possesses an enormous specific surface area and is capable of offering abundant active sites for PFAS adsorption and ET.[164] However, the electrical conductivity of activated carbon is relatively limited. The granular activated carbon (GAC) cathode can achieve partial defluorination of 6:2 fluorotelomer without a catalyst at a potential of 10 V, but the defluorination rate is low.[61] Carbon nanotubes (CNTs), on the other hand, enrich PFAS and electron donors through the confinement effect, promote the generation of hydrated electrons under UV synergy, and the defluorination rate can reach more than 80% and can be reused 5 times.[165]

Metal electrodes have also been extensively studied. Hughes *et al.* used a BDD anode and Cu, Ti, and Au cathodes, separating oxidation and reduction reactions through an H-type electrolytic cell containing an agar membrane. The results showed that electrochemical reduction contributed significantly to the total degradation of GenX, accounting for 52% with the Cu cathode, 66% with the Ti cathode, and 92% with the Au cathode.[156]

In recent years, modified electrodes have become a research hotspot. For example, cathodes modified with quaternary ammonium salt surfactants can surmount the electrostatic repulsion between anionic PFAS compounds and the cathode through hydrophobic interactions and electrostatic interactions, promote the adsorption of PFAS on the cathode surface, and significantly improve the reduction efficiency. Wang *et al.* studied the ER system equipped with a quaternary ammonium surfactant-functionalized cathode for the degradation of PFMeUPA. At −1.6 V (*vs.* Ag/AgCl), the cathode modified with OTAB achieved a removal rate of 99.81% and a defluorination rate of 78.67%. Among them, PFMeUPA is initially adsorbed on the modified cathode surface through hydrophobic and electrostatic interactions. DET induces the cleavage of C–F bonds, and the C=C structure of PFAS contributes to the fragmentation of C–F bonds. The degradation pathway comprises sequential reductive defluorination and hydrogenation. This work uncovers the critical role of quaternary ammonium surfactants in electron transfer and electrocatalytic performance, providing an innovative strategy for remediating PFAS-contaminated groundwater.[53]

While surfactant modifications partially mitigate this issue by promoting hydrophobic interactions, achieving true defluorination requires a deeper microstructural intervention. Constructing 2D layered confinement structures, such as MXenes or hierarchically structured carbon networks, offers a microenvironment where local electrostatic fields and steric effects are drastically altered. These interlayer channels or molecular-level pores act as nanoreactors. When PFAS molecules intercalate into these confined spaces, the spatial restriction prevents the premature desorption of partially hydrodefluorinated intermediates. Consequently, the local concentration of both the target pollutants and reactive species is maximized, ensuring that stepwise C–F bond cleavage is driven to completion, ultimately advancing the process from preliminary parent compound removal to comprehensive structural destruction.

In addition to surfactant modification, researchers have further optimized electrode performance by means of loading nanocatalysts on the electrode surface and preparing composite material electrodes. Graphene, with its unique electronic structure and high specific surface area, can improve the electron transfer performance of electrodes and show good application prospects. For instance, loading transition metal nanoparticles on graphene electrodes can not only enhance the electrical conductivity of the electrodes but also provide more catalytically active sites, thereby improving the degradation capacity of PFAS. For example, Li *et al.* prepared reduced graphene oxide aerogels (rGA) using a microbubble template method, and loaded Fe_3O_4 and Cu nanoparticles to obtain Fe_3O_4-rGA and Cu-rGA as cathodes. These cathodes were combined with BDD electrodes to construct a heterogeneous Fenton-like system. Through the synergistic effect between rGA loaded with Fe_3O_4 or Cu NPs and BDD electro-oxidation, the abundant active sites promoted the generation of ·OH. In combination with the BDD anode, which has a high OEP, a wide electrochemical window, and an inert surface without secondary pollution, the synergistic effect of the two enabled the removal rate of PFOA to reach over 98% within 360 minutes and complete removal within 720 minutes, with the F^- generation rate exceeding 60%. Moreover, the energy consumption and cost are relatively low.[152]

Zhang *et al.* explored that the ZIF-67 modified cathode could achieve a defluorination rate of 97.16% at a voltage of -1.2 V *vs.* Ag/AgCl. Its core advantage lies in the efficient catalytic generation of H by the Co–N structure, which promotes defluorination through the synergistic effect of direct reduction and H-mediated indirect reduction. The introduction of carbon black enhances the electrical conductivity and adsorption performance of the electrode. DFT calculations confirmed that the Co–N structure with low nitrogen content is more conducive to the generation and adsorption of H, providing a new method for the efficient removal of short-chain PFAS.[155]

Loading nanoparticles such as precious metals or transition metals on the electrode surface can utilize the high catalytic activity of metals to effectively reduce the activation energy of the reaction, accelerating the cleavage of C–F bonds and the mineralization of PFAS.[166] In addition, after introducing non-precious metal catalysts into the electrode system, they can achieve efficient adsorption and catalytic oxidation of PFAS by virtue of their special electronic structure and surface properties.

5.2.2 **Other factors.** Short-chain PFAS, with their lower molecular weight and greater hydrophilicity compared to long-chain counterparts, exhibit reduced adsorption at cathode surfaces and are less likely to accumulate at reactive sites. This presents a challenge in ensuring efficient electron transfer and reduction under typical experimental conditions. To optimize ER for short-chain PFAS, electrode materials must incorporate features that enhance both adsorption and reactivity. The development of materials with high surface area and modified surface chemistry can improve PFAS adsorption, especially by introducing functional groups that enhance the interaction with the hydrophilic headgroups of short-chain PFAS. Additionally, incorporating conductive polymers or ion-exchange materials that can promote selective adsorption of anionic species and facilitate the generation of e_{aq}^- or ·H species will enhance the reduction process. It is also important to optimize the cathode's microstructure to allow for fast mass transport and prevent blocking of reactive sites by large volumes of water or competing ions. By adjusting these parameters, ER electrodes can be more effective at breaking down short-chain PFAS at low concentrations, offering a promising solution for tackling these challenging contaminants.

The structural characteristics of PFAS molecules affect ER efficiency. Their specific functional groups significantly influence their electron-accepting capacity and reaction pathways. For example, PFAS containing C=C structures can promote the cleavage of C–F bonds and accelerate the reduction reaction. In addition, intermediate free radicals generated in the ER can further react with PFAS molecules, promoting the defluorination process. The electron cloud distribution on the cathode surface and the spatial configuration of PFAS molecules directly affect ET efficiency and reaction selectivity. Theoretical calculations reveal the microscopic interaction mechanism between PFAS and the electrode surface by simulating molecular orbital interactions. At high concentrations, PFAS tend to form micelles/semi-micelles, which reduce mobility and hinder degradation. Therefore, it is necessary to control the concentration or optimize the electrode surface to enhance adsorption.

The type and concentration of electrolytes are crucial for solution conductivity, the generation of active species, and reaction kinetics. When Na_2SO_4 is used as the electrolyte, electrochemical activation can generate $SO_4^{\bullet -}$ and ·OH, which participate in PFAS degradation. Inert electrolytes need to have a high ionic strength and a wide potential window. Studies have shown that Na_2SO_4 is more effective than $NaClO_4$ and has less environmental impact. For example, Saleh *et al.* systematically studied the effects of 17 types of saltwater electrolytes on the electrocatalytic conversion of PFOA, confirming that the increase in electrolyte concentration and conductivity accelerates degradation. The addition of Cl^- has no significant effect, while NO_3^- reduces efficiency. The degradation of PFOA is not affected by the pH of the bulk solution, and there is a good correlation between conductivity and degradation rate, providing an important basis for electrolyte optimization. Mixed electrolytes can balance cost and efficiency, but it is necessary to avoid the generation of chlorine-oxygen free radicals (·ClO) that may cause side reactions.[167]

The pH value affects the existing forms of PFAS and the charge properties of the electrode surface. Alkaline conditions inhibit HER, and OH^- will participate in the reaction to generate superoxide free radicals, which affects the degradation products and degradation efficiency. Acidic conditions enhance hydrophobic interactions, and some PFAS are more likely to gain electrons and be reduced, but it is necessary to balance the dissociation state of PFAS.

A higher *j* can provide more electrons per unit time, which can accelerate the rate of the reduction reaction in the initial stage.[33] However, an excessively high *j* will trigger side reactions such as HER, consuming electrons and reducing the energy efficiency of PFAS degradation.[61] Studies by Ma *et al.* showed that when a direct current of 0.3 V was applied, the

Table 4 Technologies and experimental conditions for degrading PFAS in recent years[a]

Technologies	PFAS	Experiment conditions	Energy consumption	PFAS removal (%)	Defluorination (%)	Ref.
AO/Rotation	PFOA	BDD anode produced bubbles, 4.5 V/SHE, 9 h, 48 μM	7 kWh m^{-3} log^{-1}	99	93	176
AO/Rotation	PFOA	BDD anode alone, 4.5 V/SHE, 9 h, 48 μM	13 kWh m^{-3} log^{-1}	99	82	176
AO/Rotation	PFOA	BDD anode, 100 mL per min N_2, 4.5 V/SHE, 5 h, 48 μM	9.2 kWh m^{-3} log^{-1}	99	98	176
EC-EO	PFCAs PFSAs	Anode EC/EO:Zn/Ti_4O_7, cathode: Stainless steel		>90		177
NF-EO	PFHxA	BDD/BDD, 50 A m^{-2} 20 °C 870 mg L^{-1} 20 bar	8.94 kWh m^{-3} log^{-1}	98		178
GIC-adsorption-EO	PFOS	20 mA cm^{-2} 20 min	13 kWh m^{-3}	83		179
	PFOA	Mixed system		62		
	PFBA			11		
GIC-adsorption-EO	PFHpS	Anode: Graphite block	7.8 kWh m^{-3}	93.5		180
	PFHxS	Cathode: perforated stainless steel		85.7		
	PFPeS	Adsorption 20 min + regeneration 10 min		71.2		
	PFBS	19.7 V 1 A		74.7		
	PFOA			71.1		
	PFHxA			36.4		
	PFBA			2.6		
Fenton-BDD	GenX	Cathode: Gr-Ni-foam, anode: BDD/Pt/FTO, 0.05 M K_2SO_4 0.2 mM Fe^{2+}, 8–16 mA cm^{-2} 2–6 h		92.2	89	132
ZnO-EO	PFOA	Anode: Nano-ZnO-coated Ti		65.84		141
	PFOS	Cathode: Stainless steel		63.42		
	PFHpA	20 mA cm^{-2} 40 min		58.03		
	PFHxA			49.31		
Fenton-EO	PFCAs PFSAs F–53B	Anode: Ti/BDD Cathode: Pt NaCl 2 g L^{-1} 5 mA cm^{-2} 2 h	4.43–39.43 kWh m^{-3}	86.1–100		181
Fenton-EO	PFCAs PFSAs F–53B	Anode: Ti/IrO_2 Cathode: Pt NaCl 2 g L^{-1} 15 mA cm^{-2} 3 h	22.8–98.64 kWh m^{-3}	54.5–98.1		181
Redox-polymer	TFA (C2)	Activated carbon cloth electrode		89	100	20
ED-NF	PFPrA(C3)	Cellulose-based membrane filter		86	76	
	PFBA(C4)	1.0 V 10 mL min^{-1} 10 mM NaCl		90		
	PFHxA(C6)			89		
	PFOA(C8)			90		
Fenton-EO	PFOA	Anode: Ti_4O_7		92		182
	PFOS	Cathode: Carbon felt, 50 mM Na_2SO_4 5 h, 0.2 mM $FeSO_4$ pH = 3, Drum in O_2, 13 mA cm^{-2}		100		

Table 4 (*Contd.*)

Technologies	PFAS	Experiment conditions	Energy consumption	PFAS removal (%)	Defluorination (%)	Ref.
EO-ES	PFOS	Anode: BRGO	10.1 ± 0.7 kWh m^{-3}	67	75.3	37
	PFOA	Cathode: Spontex		48.6	74.1	
	PFHxS	10 mM Na_2HPO_4/NaH_2PO_4		49.1	81.1	
	PFHxA	pH = 7.2		34.2	83.3	
UV-ER	PFNA	Anode: Pt–Ti, cathode: CNT-PS-35		35.4		183
	PFOA	50 mM $NaClO_4$ UV/-2 V		33.5		
	PFOS	2 h pH = 11.5 N_2		20.4		
PE-UV-EC	PFOS	Anode: [NiFe]-layered double hydroxide	5.256 kWh m^{-3}	100		148
		Cathode: AvCarb MGL190, 8.0 M LiOH, pH = 14.9		83.3		
	PFOA	UN 254 nm 40 mW cm^{-2}, +1.6 V *vs.* RHE One cycle = 1 min ON + 5 min OFF				
PE-UV-EC	PFOS	Anode:[NiFe]–$(OH)_2$, cathode: Nifethal 70	68.2 kWh m^{-3}	100	100	184
	PFOA	8.0 M LiOH, UN 254 nm, $E_{on} = 1.6$ V 30 s, $E_{rev} = -1.74$ V 1 s				
PDC-BDD	PFOA	BDD/BDD, 7.518 g per L K_2HPO_4, 0.931 g per L KH_2PO_4 On 300 ms + Off 300 ms 8V, 30 min 20 °C 300 rpm N_2	1.95 kWh m^{-3}	56		145
ER-EO	PFOA	Co–CN_2–Fe_2O_3, -0.06 V pH = 2120 min, 0.05 M Na_2SO_4		96.1	95.9	153

[a] Perfluoroalkyl sulfonic acids (PFSAs); perfluoroheptanesulfonic acid (PFHpS); perfluoropentanesulfonic acid (PFPeS); trifluoroacetic acid (TFA); perfluoropropanoic acid (PFPrA).

removal rate of PFOA reached 63.2%, and when the voltage was 0.8 V, the removal rate increased by 2.7%. The effective enhancement of PFAS removal was achieved by strengthening electron transfer.[168]

In addition, reaction temperature and other coexisting substances in the solution can also affect the degradation process. Increasing temperature can accelerate the molecular movement rate and promote mass transfer, but it is limited by electrode stability and energy consumption.[61] However, excessively high temperatures may lead to intensified side reactions. Coexisting substances may compete with PFAS for active sites on the electrode surface and change the structure and properties of PFAS through chemical reactions, thereby affecting the degradation effect. Zeidabadi *et al.* explored the impact of organic and inorganic components such as natural organic matter (NOM), Cl^-, NO_3^-, and HCO_3^- on the degradation process. The results showed that NOM and Cl^- would inhibit PFAS degradation, while NO_3^- and HCO_3^- had little effect on degradation but significantly reduced defluorination efficiency.[169]

ER technology provides an efficient solution for PFAS degradation through the synergy of multiple pathways dominated by hydrated electrons, assisted by DET and atomic hydrogen. The design of electrode materials has expanded from precious metals to single-atom catalysts and carbon-based materials, taking both efficiency and cost into account. The optimization of electrolytes and the selection of potential windows can inhibit side reactions and improve defluorination selectivity. Future research should focus on developing anti-pollution and long-life electrodes, and further explore the impact mechanism of complex matrices in actual water bodies on the reduction pathway.

6 Combined technologies for PFAS degradation

In addressing PFAS pollution, single electrochemical technologies have various limitations, often facing issues such as high energy consumption, poor selectivity, numerous side reactions, and interference from coexisting substances.[170] However, combined systems can effectively overcome these challenges by integrating different technologies with electro-oxidation or reduction, such as nanofiltration, adsorption,[171] electrocoagulation,[172] photocatalysis,[173] Fenton's method,[174] or through innovations in electrode/system design,[175] These combinations not only reduce the overall cost but also lower the concentration of harmful by-products generated after PFAS degradation, achieving good treatment effects on groundwater with different conductivities and PFAS pollution of varying degrees,[29] Table 4 summarizes the research on the degradation of PFAS by the combination of electrochemical technology and other technologies in recent years.

The treatment efficiency can be improved by adjusting the electrode layout or utilizing reaction by-products. For example, the AO/Rotation system proposed by Wan *et al.* rotates the electrode direction by 90°, leveraging hydrogen bubbles produced *via* the cathodic hydrogen evolution reaction to deliver PFOA to the anode, thereby enhancing its oxidative degradation. Experimental results demonstrated that at a N_2 flow rate of 100 mL min^{-1}, the defluorination efficiency increased from 31% to 100% within 3 hours. Notably, the energy consumption was merely half that of the direct anodic oxidation (AO) process, while secondary pollution induced by aerosol emission was effectively avoided. This system achieved performance breakthroughs and cost reduction merely by adjusting the spatial layout of electrodes and utilizing natural bubble behavior, without the need to develop new electrode materials (Fig. 14a–c).[176]

Other studies have combined multiple treatment processes to leverage the advantages of different technologies. Shi *et al.* adopted a method combining EC and EO to treat PFAS. First, the EC process removes pollutants such as organic matter and heavy metals in wastewater, and uses cations generated by the dissolution of the zinc anode to form hydroxyl complexes that adsorb PFAS.[185] Under specific conditions, the generated foam can also promote the separation of PFASs, completing the initial concentration. In the subsequent EO stage, the Ti_4O_7 anode is used to degrade the concentrated PFAS through direct electron transfer and hydroxyl radicals. This process can efficiently separate, concentrate, and degrade PFASs in groundwater and wastewater.[177] Because the traditional method needs to go through multiple separation processes such as adsorption,

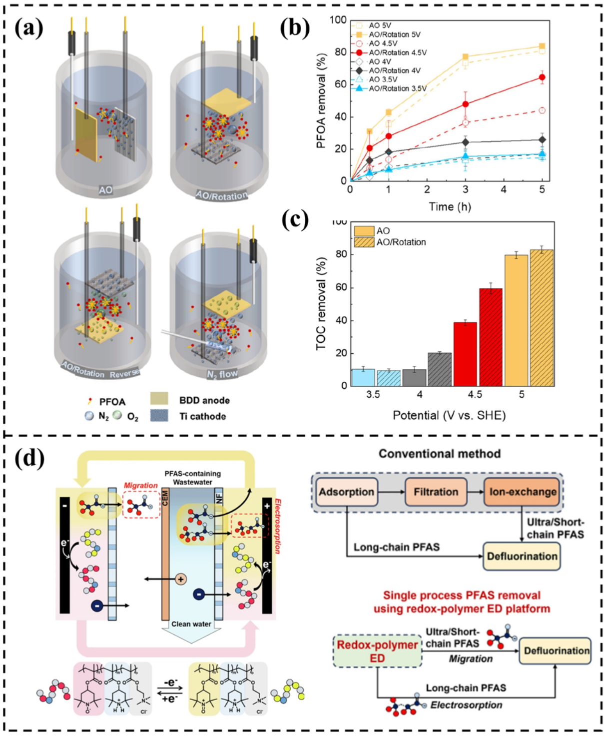

Fig. 14 (a) Schematic diagram of the AO system, AO/Rotation system. (b) Time profiles of PFOA removal. (c) TOC removal. Reproduced with permission.[176] Copyright 2023, American Chemical Society. (d) Schematic illustration of the redox-polymer ED system. Reproduced with permission.[20] Copyright 2024, Springer Nature.

filtration, ion exchange, *etc.*, and the long chain and ultra short/short chain PFAS should be treated separately, followed by defluorination, the process is very cumbersome. Kim *et al.* Comparatively studied the redox polymer electrodialysis system, which can treat PFAS while desalting through the synergistic effect of electrosorption and ion migration (Fig. 14d).[20,37] Soriano *et al.* proposed a strategy of first separating *via* NF and then electrochemically degrading the NF concentrate. Using a DowFilm NF270 membrane under a pressure of 20 bar, the rejection rate of PFHxA reached 99.4%, and the volume was reduced by 5 times in the concentration mode. Subsequently, a commercial electrochemical cell with bipolar BDD electrodes was used to treat the NF retentate. With a current density of 50 A m^{-2}, the degradation rate of PFHxA reached 98%, the total organic carbon removal rate exceeded 95%, and the energy consumption was 15.2 kWh m^3. This demonstrates the considerable potential of the combination of membrane separation and electrochemical oxidation in addressing PFAS-contaminated water.[178]

The Trzcinski team conducted studies on the treatment of PFAS by combining Graphite Intercalation Compound (GIC) adsorption with electrochemical oxidation in 2023 and 2024, respectively. In 2023, targeting PFOS, they adopted the method of GIC adsorption combined with EO. The adsorption of PFOS by GIC conformed to the Langmuir model, with a capacity of 53.9 μg g^{-1}, reaching equilibrium within 20 minutes. Adsorption was achieved through hydrophobic interactions and other mechanisms, resulting in a 99% removal rate of PFOS. However, the degradation produced short-chain by-products, making complete degradation difficult.[180] In 2024, the research was extended to PFOA and PFBS. The adsorption capacities of GIC for the three substances varied significantly: 53.9 μg g^{-1} for PFOS, 22.3 μg g^{-1} for PFOA, and 0.985 μg g^{-1} for PFBS. PFOS could be completely degraded under a current of 28 mA cm^{-2}, and the degradation rate of PFOA reached 98% at 25 mA cm^{-2}. PFBS needed to be adsorbed first before degradation. The removal rate in actual water bodies decreased by 3–40%, but under a current of 40 mA cm^{-2}, the removal rates of PFOS and PFOA could reach 95% and 68%, respectively. The advantage is that it clarifies that hydrated electrons on the GIC surface dominate the degradation and that it can handle various PFAS.[179]

Building upon the integration of adsorption and EO, such as the GIC-EO system, it is crucial to recognize that physically decoupling adsorption from degradation can still face mass transfer bottlenecks and the accumulation of recalcitrant short-chain intermediates. To truly bridge the gap between preliminary ‘removal’ and ultimate ‘mineralization’, future research must pivot towards the design of bifunctional materials that seamlessly integrate exceptional adsorption capacity with high electrocatalytic activity.

In this context, advanced porous frameworks, such as conductive molecular sieves and MXene-based carbon composites, represent a highly promising frontier. Unlike conventional adsorbents that merely concentrate pollutants, conductive molecular sieves can be engineered with precise pore architectures to selectively capture and confine PFAS molecules—including highly soluble short-chain variants—*via* size-exclusion and electrostatic interactions. Once anchored within these confined nanospaces, the structurally integrated conductive network facilitates rapid direct electron transfer and the localized generation of high-concentration ROS. This enrichment-degradation *in situ* coupling drastically prolongs the residence time of PFAS and their intermediate fragments near the catalytic active sites, effectively converting physical confinement into deep C–F bond cleavage. Similarly, 2D materials like MXenes offer tunable interlayer spacings and rich surface terminations, allowing them to act as dynamic nanoreactors that simultaneously intercalate PFAS and catalyze their destruction. Transitioning towards such bifunctional adsorbent-electrocatalysts will be a pivotal strategy for achieving complete PFAS mineralization in complex water matrices while minimizing overall energy consumption.

Other studies have focused on developing new synergistic reaction systems. Olvera-Vargas *et al.* investigated an electro-Fenton (EF) synergistic degradation system using graphene-coated nickel foam (Gr-Ni-foam) as the cathode and BDD as the anode for treating short-chain GenX. The degradation of GenX starts with DET on the BDD surface, followed by the continuous promotion of degradation by ·OH radicals generated by EF.[132] Zhang *et al.* utilized a nano-ZnO-coated Ti electrode, combining the synergistic effect of EO and photocatalytic oxidation. The nano-ZnO generates additional ·OH, which synergistically enhances with the radicals produced by EO. Its rough nanostructure also increases the electrode surface area and catalytic active sites, improving the removal efficiency.[141] Rao *et al.* developed a UV/CNT electrode system. First, PFAS is adsorbed on the electrode surface; the electrode provides instantaneous ET under negative potential to weaken the C–F bonds, and e_aq^- generated by UV photolysis of water attacks the weakened C–F bonds, significantly improving the defluorination efficiency of refractory sulfonates.[183] Huynh *et al.* explored a Fenton-assisted EO process, where H_2O_2 generated at the cathode provides raw materials for the Fenton reaction, and the anode generates ·OH and strong oxidants. Fe_3O_4 is added as a catalyst to accelerate the Fenton reaction and reduce pH requirements. Meanwhile, Fe^{3+} near the anode can be regenerated into Fe^{2+} through electroreduction, maintaining the Fenton reaction cycle and increasing the radical yield[181]

In addition, some studies have explored new electrode materials. Duinslaeger *et al.* investigated a boron-doped graphene sponge anode, which exhibited a certain removal efficiency for short-chain PFAS under low-conductivity electrolytes and single-pass low-flux mode, with low energy consumption. Moreover, this electrode is electrochemically inert to Cl^- and does not generate chlorate or perchlorate, providing possibilities for the electrochemical degradation of complex PFAS-containing wastewater and brine.[37] Gomri *et al.* studied the EO combined with EF technology using Magnéli phase Ti_4O_7 as the anode, which achieved high degradation rates of PFOA and PFOS with significantly reduced energy consumption.[182] In 2024, Meng *et al.* prepared [NiFe]-layered double hydroxide nanocatalysts *via* laser and immobilized them on a hydrophilic carbon fiber paper anode. In an 8.0 M LiOH aqueous solution, complete defluorination of PFOS was achieved through pulsed electrolysis combined with ultraviolet irradiation. The materials used are non-precious, improving the efficiency of electrical energy and capital expenditure.[148,184] Han *et al.* studied a Fe_2O_3-assisted Co–CN_2 configuration bifunctional single-atom catalyst, which can integrate reduction and oxidation processes, simultaneously inducing PFOA degradation and reducing O_2 to H_2O_2. Under the condition of −0.06 V, 96.1% PFOA degradation rate and 95.9% defluorination rate were achieved within 120 minutes, confirming the key mechanism of the synergistic effect between reduction and oxidation processes.[153]

For practical engineering applications, Specific Energy Consumption (SEC) is a critical metric for evaluating the economic viability of PFAS degradation technologies. When treating real environmental water, where PFAS concentrations are usually at trace levels, the energy efficiency of various electrochemical processes differs significantly. While standalone EO can completely cleave PFAS chains, its direct application to raw water yields a prohibitively high SEC, often ranging from tens to hundreds of kWh m^3. This is primarily because extreme trace concentrations cause severe mass transfer limitations, wasting most of the applied electrical energy on background electrolyte resistance and the competitive OER. Similarly, ER faces severe energy efficiency challenges. Although it avoids the OER, it requires high cathodic overpotentials to overcome C–F bond activation barriers, which inevitably triggers the energy-consuming HER.

In contrast, combined technologies offer a decisive energy-saving advantage through a "concentrate-and-destroy" strategy. By utilizing pre-treatment methods like membrane separation or physical adsorption, massive volumes of trace PFAS wastewater are concentrated into a significantly smaller volume of retentate or eluent. Consequently, the electrochemical module only treats this minimized volume, which exponentially enhances internal mass transfer efficiency and drastically reduces the energy wasted on parasitic side reactions.[186]

7 Conclusions

With advantages such as mild operating conditions and controllable electron transfer, electrochemical technologies have demonstrated significant potential for the degradation and remediation of PFAS. This review systematically summarizes the research progress of electrochemical technologies in PFAS destruction, exploring a research trajectory from atomic-scale bond-cleavage mechanisms and interfacial regulation in various electrochemical processes, to AI-enabled HTS, aiming to provide a reference for the further optimization of these technologies.

Regarding specific technological systems, EO exhibits notable advantages in destroying long-chain PFAS through the synergistic effects of direct electron transfer and ROS. However, its efficacy is often limited by competitive OER and the high cost of anode materials. Conversely, ER provides an alternative pathway to overcome oxidative barriers and achieve hydrogen substituted defluorination, though practical applications must address the intense electrostatic repulsion at the cathode interface and the high activation energy of C–F bonds. To mitigate the limitations of single processes, combined technologies that integrate electrochemistry with separation techniques or *in situ* adsorption have demonstrated promising synergistic effects, offering more viable engineering solutions for the pre-concentration and deep degradation of PFAS in complex water matrices.

Although considerable progress has been made in enhancing PFAS degradation efficiency in recent years, several technical challenges remain in practical applications. Notably, it is crucial to recognize that a high parent compound removal rate does not strictly equate to complete mineralization. During the degradation process, the accumulation of short-chain intermediates frequently occurs. Because these short-chain species possess weaker hydrophobicity and encounter higher electrostatic repulsion barriers, effectively mitigating their escape to achieve deep defluorination remains a critical issue that current electrochemical technologies must address.

To address these challenges, future electrode material design might increasingly focus on the confinement effects of micro-interfaces and bifunctional synergy. Relying solely on macroscopic physical adsorption or solitary electrocatalysis often presents limitations in achieving deep mineralization. Developing bifunctional materials that seamlessly integrate specific adsorption-enrichment with high electrocatalytic activity represents a highly promising direction for in-depth exploration. Through size exclusion, hydrogen bonding, or electrostatic interactions within microscopic pores, such materials are expected to anchor short-chain PFAS *in situ* while simultaneously concentrating reactive species near the catalytic active sites. This modulation of the microenvironment helps alleviate mass transfer limitations and facilitates the transition of PFAS from physical surface enrichment to deep structural destruction.

Furthermore, navigating the vast and complex compositional space of materials *via* conventional trial-and-error methods is often excessively time-consuming. The introduction of AI-enabled HTS closed-loop systems offers a more efficient approach for the rapid development of multi-objective electrode materials. Future research could attempt to more tightly couple intrinsic mechanistic descriptors derived from theoretical calculations with machine learning models. This integration would allow for the simultaneous pursuit of high degradation activity while comprehensively balancing side-reaction suppression, target pollutant affinity, and long-term stability.

Overall, achieving the complete and harmless destruction of PFAS remains a long-term and complex endeavor. Narrowing the gap between ideal laboratory conditions and realistic, complex water matrices remains a focal point for future research. With a deepening understanding of microscopic confined mineralization mechanisms and the progressive application of data-driven design, electrochemical technologies are poised to play an increasingly active and robust role in the practical remediation of PFAS and other emerging contaminants.

Author contributions

Yuqing Dong: conceptualization, methodology, data curation, writing – original draft, writing – review & editing. Shuaiyu Gao: conceptualization, methodology. Yuelin Zhao: validation, data curation. Genban Sun: writing – review & editing, project administration, funding acquisition. Jihong Yu: conceptualization, methodology, writing – review & editing, project administration, funding acquisition.

Conflicts of interest

There are no conflicts to declare.

Data availability

No primary research results, software or code have been included, and no new data were generated or analyzed as part of this review.

Acknowledgements

We thank the Fundamental and Interdisciplinary Disciplines Breakthrough Plan of the Ministry of Education of China (JYB2025XDXM903), the National Natural Science Foundation of China (22288101, 22271018, 22571020), the '111 Center' (B17020).

Notes and references

1 J. Wang, C. Cao, Y. Zhang, Y. Zhang and L. Zhu, *Appl. Catal., B*, 2021, **286**, 119911.
2 S. Yin, J. F. López, C. Sandoval-Pauker, J. J. Calvillo Solís, S. Glass, A. Habib, W.-Y. Lee, M. S. Wong, P. J. J. Alvarez and D. Villagrán, *Appl. Catal., Bc*, 2024, **355**, 124136.
3 M. Liao, S. Zhao, G. Zhan, J. Liang, Z. Li, F. Dong, Y. Pan, H. Li and L. Zhang, *J. Am. Chem. Soc.*, 2025, **147**, 3402–3411.
4 J. S. Ko, N. Q. Le, D. R. Schlesinger, D. Zhang, J. K. Johnson and Z. Xia, *Sci. Rep.*, 2021, **11**, 19014.
5 H. Song, L. Yan, J. Ma, J. Jiang, G. Cai, W. Zhang, Z. Zhang, J. Zhang and T. Yang, *Water Res.*, 2017, **116**, 182–193.
6 C. E. Schaefer, C. Andaya, A. Urtiaga, E. R. McKenzie and C. P. Higgins, *J. Hazard. Mater.*, 2015, **295**, 170–175.
7 C. E. Schaefer, S. Choyke, P. L. Ferguson, C. Andaya, A. Burant, A. Maizel, T. J. Strathmann and C. P. Higgins, *Environ. Sci. Technol.*, 2018, **52**, 10689–10697.
8 J. Hou, G. Li, M. Liu, L. Chen, Y. Yao, P. H. Fallgren and S. Jin, *Chemosphere*, 2022, **287**, 132205.
9 A. Román Santiago, S. Yin, J. Elbert, J. Lee, D. Shukla and X. Su, *J. Am. Chem. Soc.*, 2023, **145**, 9508–9519.
10 O. E. Beyioku, A. Gilboa and A. Ronen, *Sep. Purif. Technol.*, 2025, **372**, 133457.
11 R. Ahmad, X. Liu, H. N. Ilyas, P. Hanphaiboon, W. Wang, M. Noman, B. Pan and Y. Wang, *Sep. Purif. Technol.*, 2025, **367**, 132797.
12 J. Hu, S. Wang, J. Yu, W. Nie, J. Sun and S. Wang, *Environ. Sci. Technol.*, 2021, **55**, 1260–1269.
13 S. Verma, R. S. Varma and M. N. Nadagouda, *Sci. Total Environ.*, 2021, **794**, 148987.
14 M. S. Samuel, G. Kadarkarai, D. R. Ryan, S. T. McBeath, B. K. Mayer and P. J. McNamara, *Sci. Total Environ.*, 2024, **942**, 173736.
15 P. Gogoi, Y. Yao and Y. C. Li, *ChemElectroChem*, 2022, **10**, e202201006.
16 A. Menezes, L. C. Goveas, R. Vinayagam and R. Selvaraj, *J. Water Process Eng.*, 2025, **69**, 106621.
17 N. Liu, Y. Li, M. Zhang, N. Che, X. Song, Y. Liu and C. Li, *Sci. Total Environ.*, 2024, **946**, 174223.
18 R. Singh, U. T. Uthappa, Y.-H. Ahn and S. S. Ray, *Inorg. Chem. Commun.*, 2025, **178**, 114614.
19 L. Jiang, R. Cao, Z. Huang, J. Jin, Z. Du and H. Li, *Chem. Eng. J.*, 2024, **502**, 158161.
20 N. Kim, J. Elbert, E. Shchukina and X. Su, *Nat. Commun.*, 2024, **15**, 8321.
21 Z. Lin, M. S. Ersan, S. Garcia-Segura, F. Perreault and P. Westerhoff, *RSC Adv.*, 2024, **14**, 15627–15636.
22 J. Niu, H. Lin, C. Gong and X. Sun, *Environ. Sci. Technol.*, 2013, **47**, 14341–14349.
23 L. I. FitzGerald, J. F. Olorunyomi, R. Singh and C. M. Doherty, *ChemSusChem*, 2022, **15**, e202201136.
24 A. L. Junker, J.-M. A. Juve, L. Bai, C. S. Qvist Christensen, L. Ahrens, I. T. Cousins, M. Ateia and Z. Wei, *Environ. Sci. Technol.*, 2025, **59**, 8939–8950.
25 J.-M. Arana Juve, B. Wang, M. S. Wong, M. Ateia and Z. Wei, *Curr. Opin. Chem. Eng.*, 2023, **41**, 100943.
26 X. Chen, T. Yuan, X. Yang, S. Ding and M. Ma, *Catalysts*, 2023, **13**, 1308.
27 M. K. Wilsey, T. Taseska, Z. Meng, W. Yu and A. M. Müller, *Chem. Commun.*, 2023, **59**, 11895–11922.
28 A. Dube, S. J. Malode, H. Akhdar, A. N. Alodhayb and N. P. Shetti, *Colloids Surf., B*, 2025, **252**, 114653.
29 S. Sharma, N. P. Shetti, S. Basu, M. N. Nadagouda and T. M. Aminabhavi, *Chem. Eng. J.*, 2022, **430**, 132895.
30 Z. Meng, M. K. Wilsey and A. M. Müller, *ACS Catal.*, 2024, **14**, 16577–16588.
31 H. Lin, R. Xiao, R. Xie, L. Yang, C. Tang, R. Wang, J. Chen, S. Lv and Q. Huang, *Environ. Sci. Technol.*, 2021, **55**, 2597–2607.
32 Q. Zhuo, S. Deng, B. Yang, J. Huang, B. Wang, T. Zhang and G. Yu, *Electrochim. Acta*, 2012, **77**, 17–22.
33 S. Sukeesan, N. Boontanon and S. K. Boontanon, *Environ. Technol. Innovation*, 2021, **23**, 101655.
34 H. Lin, J. Niu, J. Xu, H. Huang, D. Li, Z. Yue and C. Feng, *Environ. Sci. Technol.*, 2013, **47**, 13039–13046.
35 Y. Su, U. Rao, C. M. Khor, M. G. Jensen, L. M. Teesch, B. M. Wong, D. M. Cwiertny and D. Jassby, *ACS Appl. Mater. Interfaces*, 2019, **11**, 33913–33922.
36 B. Yang, J. Wang, C. Jiang, J. Li, G. Yu, S. Deng, S. Lu, P. Zhang, C. Zhu and Q. Zhuo, *Chem. Eng. J.*, 2017, **316**, 296–304.
37 N. Duinslaeger and J. Radjenovic, *Water Res.*, 2022, **213**, 118148.
38 X. Duan, W. Wang, Q. Wang, X. Sui, N. Li and L. Chang, *Chemosphere*, 2020, **260**, 127587.

39 D. Huang, K. Wang, J. Niu, C. Chu, S. Weon, Q. Zhu, J. Lu, E. Stavitski and J.-H. Kim, *Environ. Sci. Technol.*, 2020, **54**, 10954–10963.

40 S. Sinha, A. Chaturvedi, R. K. Gautam and J. J. Jiang, *J. Am. Chem. Soc.*, 2023, **145**, 27390–27396.

41 J. J. Calvillo Solís, C. Sandoval-Pauker, D. Bai, S. Yin, T. P. Senftle and D. Villagrán, *J. Am. Chem. Soc.*, 2024, **146**, 10687–10698.

42 D. Song, B. Qiao, X. Wang, L. Zhao, X. Li, P. Zhang, Y. Yao, H. Chen, L. Zhu and H. Sun, *Environ. Sci. Technol.*, 2023, **57**, 9416–9425.

43 J. Hu, X. Yang, X. Song, Y. Miao, Y. Yu, W. Xiang, M. Huang, W. Wu, K. Liang, S. Zhao and H. Liu, *J. Hazard. Mater.*, 2024, **480**, 136283.

44 J. E. Zenobio, O. A. Salawu, Z. Han and A. S. Adeleye, *J. Hazard. Mater. Adv.*, 2022, **7**, 100130.

45 F. Jiang, M. Wu, Z. Zhu, C. Jiang, Z. Ai and J. Gong, *Water Res.*, 2025, **284**, 124049.

46 N. Loganathan, C. E. Schumm, M. K. O'Reilly and A. K. Wilson, *Environ. Sci. Technol.*, 2025, **59**, 14637–14648.

47 Y. Wang, R. D. Pierce, H. Shi, C. Li and Q. Huang, *Environ. Sci.:Water Res. Technol.*, 2020, **6**, 144–152.

48 B. B. de Souza and J. Meegoda, *Sci. Total Environ.*, 2024, **926**, 171738.

49 M. J. Bentel, Y. Yu, L. Xu, Z. Li, B. M. Wong, Y. Men and J. Liu, *Environ. Sci. Technol.*, 2019, **53**, 3718–3728.

50 S. Biswas and B. M. Wong, *ACS ES&T Eng.*, 2023, **4**, 96–104.

51 J. Blotevogel, R. J. Giraud and T. Borch, *Chem. Eng. J.*, 2018, **335**, 248–254.

52 M. S. Mohamed, B. P. Chaplin and A. A. Abokifa, *ACS Omega*, 2024, **9**, 44532–44541.

53 Y. Wang, Y. Xiao, Y. Wang, Q. Lin, Y. Zhu, Z. Ni and R. Qiu, *Environ. Sci. Technol.*, 2023, **57**, 7578–7589.

54 Y. Wang, L. Li, Y. Wang, H. Shi, L. Wang and Q. Huang, *Chem. Eng. J.*, 2022, **431**, 13929.

55 J. Ma, Y. Wang, H. Xu, M. Ding and L. Gao, *Process Saf. Environ. Prot.*, 2022, **168**, 275–284.

56 X. Zhang, J. Nan, H. Zhang, P. Li and X. Lin, *Water Res.*, 2025, **286**, 124182.

57 S. Raghavan, B. P. Chaplin and S. Mehraeen, *J. Phys. Chem. C*, 2025, **129**, 10027–10037.

58 Y. Wang, J. Zhang, W. Zhang, J. Yao, J. Liu, H. He, C. Gu, G. Gao and X. Jin, *Angew. Chem., Int. Ed.*, 2024, **63**, e202402440.

59 Y. Chen, Y. Yang, J. Cui, H. Zhang and Y. Zhao, *J. Hazard. Mater.*, 2024, **465**, 133260.

60 B. Yan, R. Alessandri, S. J. Marrink, L. S. Lee and J. Liu, *Environ. Sci. Technol. Lett.*, 2025, **12**, 626–631.

61 D. Ackerman Grunfeld, A. M. Jones, J. Sun, S. T. Le, R. Pickford, Q. Huang, M. Manefield, N. Kumar, M. J. Lee and D. M. O'Carroll, *Environ. Sci.:Water Res. Technol.*, 2024, **10**, 272–287.

62 J. A. R. Willemsen and I. C. Bourg, *J. Colloid Interface Sci.*, 2021, **585**, 337–346.

63 B. G. Lamb and B. Ma, *Nanoscale*, 2025, **17**, 10632–10643.

64 S. Kancharla, A. Choudhary, R. T. Davis, D. Dong, D. Bedrov, M. Tsianou and P. Alexandridis, *J. Hazard. Mater.*, 2022, **428**, 128137.

65 Y. Yang, *Front. Environ. Sci. Eng.*, 2020, **14**, 85.

66 K. Wang, R. Wang, W. Shan, Z. Yang, Y. Chen, L. Wang and Y. Zhang, *Environ. Sci. Technol.*, 2024, **58**, 22766–22776.

67 F. Ecke, B. Ytrehus, M. Evander, B. Hörnfeldt, A. Leijon, J. Malmsten, A. Skrobonja and L. Ahrens, *Sci. Rep.*, 2025, **15**, 31003.

68 Y. Zhang, J. Liu, A. Moores and S. Ghoshal, *Environ. Sci. Technol.*, 2020, **54**, 4631–4640.

69 B. Xu, G. Wu, Z. Li, G. Xu, H. Zeng, R. Tong and H. Y. Ng, *npj Clean Water*, 2025, **8**, 82.

70 G. Xu, Y. Li, J. Li, J. Li, X. Liu, C. Wang, W. Mai, G. Yang and L. Pan, *Angew. Chem., Int. Ed.*, 2025, **64**, e202511389.

71 C. S. Tshangana, S. T. Nhlengethwa, S. Glass, S. Denison, A. T. Kuvarega, T. T. I. Nkambule, B. B. Mamba, P. J. J. Alvarez and A. A. Muleja, *npj Clean Water*, 2025, **8**, 41.

72 R. Sun, J. Cao, A. A. Dolatabad, L. Zhao, J. Mai, X. Zhang and F. Xiao, *npj Emerg. Contam.*, 2025, **1**, 10.

73 Y. Chen, Z. Guo, M. Angelaki, Y. Carreira Mendes Da Silva, J. Song, W. Wu, J. Lin, A. Gandolfo, J. Chen and C. George, *J. Am. Chem. Soc.*, 2025, **147**, 33754–33760.

74 D. Xia, H. Zhang, Y. Ju, H.-b. Xie, L. Su, F. Ma, J. Jiang, J. Chen and J. S. Francisco, *J. Am. Chem. Soc.*, 2024, **146**, 11266–11271.

75 Y. Zhang, Y. Zhi, J. Liu and S. Ghoshal, *Environ. Sci. Technol.*, 2018, **52**, 6300–6308.

76 Z. Fu, P. Huang, X. Wang, W. D. Liu, L. Kong, K. Chen, J. Li and Y. Chen, *Adv. Energy Mater.*, 2025, **15**, 2500744.

77 T. Araki, H. Ota, Y. Murata, Y. Sumii, J. Hamaura, H. Adachi, T. Kagawa, H. Hori, J. Escorihuela and N. Shibata, *Nat. Commun.*, 2025, **16**, 6526.

78 A. N. Garcia, Y. Zhang, S. Ghoshal, F. He and D. M. O'Carroll, *Environ. Sci. Technol.*, 2021, **55**, 8464–8483.

79 Y. Zhang, J. Tang, Z. Ni, Y. Zhao, F. Jia, Q. Luo, L. Mao, Z. Zhu and F. Wang, *J. Phys. Chem. Lett.*, 2021, **12**, 5279–5285.

80 W. Ding, T. Tang, X. Tan and Y. Huang, *Environ. Sci. Technol.*, 2025, **59**, 17899–17908.

81 Y. Wang, H. Xu and R. Li, *Sci. Rep.*, 2025, **15**, 21023.

82 S. Yaghoobian, M. A. Ramirez-Ubillus, L. Zhai and J.-H. Hwang, *Chem. Sci.*, 2025, **16**, 13564–13573.

83 Y. Zhang, A. Moores, J. Liu and S. Ghoshal, *Environ. Sci. Technol.*, 2019, **53**, 8672–8681.

84 W. Ding, X. Tan, G. Chen, J. Xu, K. Yu and Y. Huang, *ACS Appl. Mater. Interfaces*, 2021, **13**, 41584–41592.

85 M. Hattori, D. Saha, M. Z. Bacho and N. Shibata, *Nat. Chem.*, 2025, **17**, 1480–1487.

86 Y. Huang and A. A. Keller, *ACS Sustainable Chem. Eng.*, 2013, **1**, 731–736.

87 D. Wang, X. Liu, Z. Guo, W. Shan, Z. Yang, Y. Chen, F. Ju and Y. Zhang, *Environ. Sci. Technol.*, 2024, **58**, 20160–20171.

88 Y. Yang, J. Wu, Z. Luo, X. Jia, G. Jiang and F. Wang, *J. Am. Chem. Soc.*, 2025, **147**, 32537–32547.

89 Y. Shi, M. Sun, H. Shi, Z. Liang, B. Qiao, S. Zhao, X. Pu and D. Song, *Sci. Bull.*, 2025, **70**, 3058–3089.

90 Z. Wang, Y. Zhang, B. Liu, K. Wu, S. Thevuthasan, D. R. Baer, Z. Zhu, X.-Y. Yu and F. Wang, *Anal. Chem.*, 2016, **89**, 960–965.
91 M. Ahmadi, O. Adeleye, G. Vonalt and M. Nazemi, *Environ. Sci. Technol.*, 2025, **59**, 17952–17977.
92 Y. Wang, C. Tang, T. Xiao, F. Xiong, X. Zhou, K. Zhang and J. Gong, *J. Energy Chem.*, 2025, **110**, 728–739.
93 M. Rittiruam, J. Noppakhun, S. Setasuban, N. Aumnongpho, A. Sriwattana, S. Boonchuay, T. Saelee, C. Wangphon, A. Ektarawong, P. Chammingkwan, T. Taniike, S. Praserthdam and P. Praserthdam, *Sci. Rep.*, 2022, **12**, 16653.
94 E. R. Pezoulas, B. Tajdini, Y. Ko, A. A. Uliana, R. Giovine, H. Furukawa, H. Vatankhah, J. Börgel, K. C. Kim, C. Bellona and J. R. Long, *J. Am. Chem. Soc.*, 2025, **147**, 21832–21843.
95 J. Benavides-Hernández and F. Dumeignil, *ACS Catal.*, 2024, **14**, 11749–11779.
96 Y. He, J. Zhou, Y. Li, Y.-D. Yang, J. L. Sessler and X. Chi, *J. Am. Chem. Soc.*, 2024, **146**, 6225–6230.
97 R.-R. Liang, S. Xu, Z. Han, Y. Yang, K.-Y. Wang, Z. Huang, J. Rushlow, P. Cai, P. Samorì and H.-C. Zhou, *J. Am. Chem. Soc.*, 2024, **146**, 9811–9818.
98 D. J. Lea-Smith, F. Hassard, F. Coulon, N. Partridge, L. Horsfall, K. D. J. Parker, R. D. J. Smith, R. R. McCarthy, B. McKew, T. Gutierrez, V. Kumar, G. Dotro, Z. Yang, T. P. Curtis, P. Golyshin, S. Heaven, B. Jefferson, P. Jeffrey, D. L. Jones, K. Le Corre Pidou, Y. Liu, T. Lyu, C. Smith, A. Yakunin, Y. Zhang and N. Krasnogor, *Nat. Commun.*, 2025, **16**, 3538.
99 J. Wang and Y. Zhang, *Next Mater.*, 2025, **9**, 100993.
100 F. Dikmen, A. Demir, B. Özkaya, M. O. Raza, J. Rasheed, T. Asuroglu and S. Alsubai, *Sci. Rep.*, 2025, **15**, 25347.
101 I. Peivaste, S. Belouettar, F. Mercuri, N. Fantuzzi, H. Dehghani, R. Izadi, H. Ibrahim, J. Lengiewicz, M. Belouettar-Mathis, K. Bendine, A. Makradi, M. Horsch, P. Klein, M. E. Hachemi, H. A. Preisig, Y. Rezgui, N. Konchakova and A. Daouadji, *Compos. Struct.*, 2025, **372**, 119419.
102 R. Batra, L. Song and R. Ramprasad, *Nat. Rev. Mater.*, 2020, **6**, 655–678.
103 A. O. C. Iroegbu, M. L. Teffo, E. R. Sadiku, R. Meijboom and S. P. Hlangothi, *npj Clean Water*, 2025, **8**, 85.
104 N. Jeong, S. Park, S. Mahajan, J. Zhou, J. Blotevogel, Y. Li, T. Tong and Y. Chen, *Nat. Commun.*, 2024, **15**, 10918.
105 M. A. Ismail, A. G. Taki, S. Kumar, S. S. Sammen, A. Amari, A. Bongale, O. Kisi and A. Salem, *Sci. Rep.*, 2025, **15**, 9439.
106 K. Muta, K. Okamoto, H. Nakayama, S. Wada and A. Nagaki, *Nat. Commun.*, 2025, **16**, 416.
107 Z. Chen, Z. Wei, Z. Yang, Y. Chen and Y. Zhang, *Environ Sci. Technol.*, 2025, **59**, 18990–19001.
108 Y. Liang, L. Yang, C. Tang, Y. Yang, S. Liang, A. Wang, J. Xu, Q. Huang and H. Lin, *Nat. Commun.*, 2025, **16**, 1972.
109 A. Nandy, A. Rana, N. Shibata and S. Banerjee, *J. Am. Chem. Soc.*, 2025, **147**, 22542–22549.
110 J. Yin, W. Li, H. Chen, J. Qiu, H. Feng, X. Xu, Q. Jin and X. Wang, *ACS Catal.*, 2025, **15**, 15754–15764.
111 Z. Chen, J. Chen, S. Tan, Z. Yang and Y. Zhang, *Environ. Sci. Technol.*, 2024, **58**, 2542–2553.
112 Y. Wu, K. Pei, J. Zhou, J. Xiong, Y. Liu, P. Li, F. Li, J. Wang, X. Liu, M. Deng and C. Wu, *Sci. Rep.*, 2025, **15**, 26141.
113 B. T.-W. Tan, N. H. H. Abu Bakar and H. L. Lee, *J. Environ. Chem. Eng.*, 2025, **13**, 114990.
114 M. Mirabediny, J. Sun, T. T. Yu, B. Åkermark, B. Das and N. Kumar, *Chemosphere*, 2023, **321**, 138109.
115 J. Radjenovic, N. Duinslaeger, S. S. Avval and B. P. Chaplin, *Environ. Sci. Technol.*, 2020, **54**, 14815–14829.
116 S. T. McBeath, A. Serrano Mora, F. Asadi Zeidabadi, B. K. Mayer, P. McNamara, M. Mohseni, M. R. Hoffmann and N. J. D. Graham, *Curr. Opin. Electrochem.*, 2021, **30**, 100865.
117 S. Giannakis, K.-Y. A. Lin and F. Ghanbari, *Chem. Eng. J.*, 2021, **406**, 127083.
118 M. Gar Alalm and D. C. Boffito, *Chem. Eng. J.*, 2022, **450**, 138352.
119 J. López-Vázquez, C. S. Santos, R. Montes, R. Rodil, J. B. Quintana, J. Gäbler, L. Schäfer, F. C. Moreira and V. J. P. Vilar, *Chem. Eng. J.*, 2024, **482**, 148925.
120 M. Veciana, J. Bräunig, A. Farhat, M.-L. Pype, S. Freguia, G. Carvalho, J. Keller and P. Ledezma, *J. Hazard. Mater.*, 2022, **434**, 128886.
121 C. E. Schaefer, C. Andaya, A. Burant, C. W. Condee, A. Urtiaga, T. J. Strathmann and C. P. Higgins, *Chem. Eng. J.*, 2017, **317**, 424–432.
122 C. Wang, T. Zhang, L. Yin, C. Ni, J. Ni and L.-A. Hou, *Chemosphere*, 2022, **286**, 131804.
123 Z. Chen, X. Wang, H. Feng, S. Chen, J. Niu, G. Di, D. Kujawski and J. C. Crittenden, *Environ. Sci. Technol.*, 2022, **56**, 14409–14417.
124 L. Zhao, R. Pu, S. Deng, L. Lin, D. Mantzavinos, R. Naidu, C. Fang and Y. Lei, *Sep. Purif. Technol.*, 2025, **359**, 130459.
125 M. Pierpaoli, M. Szopińska, B. K. Wilk, M. Sobaszek, A. Łuczkiewicz, R. Bogdanowicz and S. Fudala-Książek, *J. Hazard. Mater.*, 2021, **403**, 123606.
126 H. Zhao, J. Gao, G. Zhao, J. Fan, Y. Wang and Y. Wang, *Appl. Catal., B*, 2013, **136–137**, 278–286.
127 A. L. Tasca, J. N. Uwayezu, I. Carabante and J. Kumpiene, *J. Environ. Chem. Eng.*, 2025, **13**, 117044.
128 L. Bu, S. Zhu and S. Zhou, *Chemosphere*, 2018, **195**, 236–244.
129 Q. Zhuo, J. Wang, J. Niu, B. Yang and Y. Yang, *Chem. Eng. J.*, 2020, **379**, 122280.
130 Y. Liu, X. Fan, X. Quan, Y. Fan, S. Chen and X. Zhao, *Environ. Sci. Technol.*, 2019, **53**, 5195–5201.
131 F. Asadi Zeidabadi, E. Banayan Esfahani, R. Moreira, S. T. McBeath, J. Foster and M. Mohseni, *Environ. Res.*, 2024, **246**, 118103.
132 H. Olvera-Vargas, Z. Wang, J. Xu and O. Lefebvre, *Chem. Eng. J.*, 2022, **430**, 132686.
133 H. Lin, J. Niu, S. Ding and L. Zhang, *Water Res.*, 2012, **46**, 2281–2289.
134 Q. Zhuo, M. Luo, Q. Guo, G. Yu, S. Deng, Z. Xu, B. Yang and X. Liang, *Electrochim. Acta*, 2016, **213**, 358–367.
135 H. Lin, J. Niu, S. Liang, C. Wang, Y. Wang, F. Jin, Q. Luo and Q. Huang, *Chem. Eng. J.*, 2018, **354**, 1058–1067.

136 J. Niu, H. Lin, J. Xu, H. Wu and Y. Li, *Environ. Sci. Technol.*, 2012, **46**, 10191–10198.
137 T. X. H. Le, H. Haflich, A. D. Shah and B. P. Chaplin, *Environ. Sci. Technol. Lett.*, 2019, **6**, 504–510.
138 Q. Zhuo, S. Deng, B. Yang, J. Huang and G. Yu, *Environ. Sci. Technol.*, 2011, **45**, 2973–2979.
139 Y. Liang, A. Wang, S. Liang, K. Sun, R. Xie, C. Zheng, S. Zhang, C. Tang, D. Cheng, J. Wang, Q. Huang and H. Lin, *Environ. Sci. Technol.*, 2025, **59**, 4745–4755.
140 C. Gomri, D. Krzyzanowski, M. Rivallin, F. Zaviska, E. Petit, M. Semsarilar and M. Cretin, *J. Environ. Chem. Eng.*, 2024, **12**, 113495.
141 C. Zhang, J. Tang, C. Peng and M. Jin, *J. Mol. Liq.*, 2016, **221**, 1145–1150.
142 Q. Zhuo, Q. Xiang, H. Yi, Z. Zhang, B. Yang, K. Cui, X. Bing, Z. Xu, X. Liang, Q. Guo and R. Yang, *J. Electroanal. Chem.*, 2017, **801**, 235–243.
143 Z. Niu, Y. Wang, H. Lin, F. Jin, Y. Li and J. Niu, *Chem. Eng. J.*, 2017, **328**, 228–235.
144 Q. Zhuo, X. Li, F. Yan, B. Yang, S. Deng, J. Huang and G. Yu, *J. Environ. Sci.*, 2014, **26**, 1733–1739.
145 R. G. H. Marks, K. Kerpen, D. Diesing and U. Telgheder, *J. Electroanal. Chem.*, 2021, **895**, 115415.
146 L. Saleh, M. Remot, Q. B. Remaury, P. Pardon, P. Labadi, H. Budzinski, C. Coutanceau and J.-P. Croué, *Chem. Eng. J.*, 2024, **489**, 151255.
147 S. Li, Q. Wang, L. Lyu and J. Leng, *Microchem. J.*, 2025, **213**, 113789.
148 Z. Meng, M. K. Wilsey, C. P. Cox and A. M. Müller, *J. Catal.*, 2024, **431**, 115403.
149 A. B. Nienhauser, M. S. Ersan, Z. Lin, F. Perreault, P. Westerhoff and S. Garcia-Segura, *J. Environ. Chem. Eng.*, 2022, **10**, 107192.
150 Y. Luo, O. S. Awoyemi, S. Gopalan, A. Nolan, F. Robinson, J. Fenstermacher, L. Xu, J. Niu, M. Megharaj, R. Naidu and C. Fang, *J. Cleaner Prod.*, 2023, **433**, 139691.
151 T. Stahl, H. F. T. Klare and M. Oestreich, *ACS Catal.*, 2013, **3**, 1578–1587.
152 Y. Li, N. Che, N. Liu and C. Li, *Chem. Eng. J.*, 2023, **478**, 147443.
153 J. Han, M. Zhao, K. Wu, Y. Hong, T. Huang, X. Gu, Z. Wang, S. Liu and G. Zhu, *Chem. Eng. J.*, 2023, **470**, 144270.
154 J. Zhu, Y. Chen, Y. Gu, H. Ma, M. Hu, X. Gao and T. Liu, *J. Hazard. Mater.*, 2022, **422**, 126953.
155 X. Zhang, H. Wu, Y. Wang, Y. Wang, Y. Deng, Y. Zhu, S. Zhang, H. Rijnaarts, H. Bruning, J. Qin, Q. Lin, Z. Ni and R. Qiu, *Water Res.*, 2025, **268**, 122625.
156 K. Hughes, M. Pineda, S. Omanovic and V. Yargeau, *Sci. Total Environ.*, 2024, **908**, 168415.
157 L. Li, R. Guo, J. Gao, J. Liu, Z. Zhao, X. Sheng, J. Fan and F. Cui, *J. Hazard. Mater.*, 2023, **450**, 131028.
158 J. Cui, P. Gao and Y. Deng, *Environ. Sci. Technol.*, 2020, **54**, 3752–3766.
159 S. Yin, J. J. Calvillo Solís, C. Sandoval-Pauker, D. Puerto-Diaz and D. Villagrán, *J. Hazard. Mater.*, 2025, **491**, 137943.
160 H. Liu, J. Han, J. Yuan, C. Liu, D. Wang, T. Liu, M. Liu, J. Luo, A. Wang and J. C. Crittenden, *Environ. Sci. Technol.*, 2019, **53**, 11932–11940.
161 S. D. Tan, R. Y. Wang, K. M. Wang, Z. L. Yang, Y. J. Chen and Y. Y. Zhang, *Nat. Water*, 2025, **3**, 15.
162 R. Doi, M. Yasuda, N. Kajita, K. Koh and S. Ogoshi, *J. Am. Chem. Soc.*, 2023, **145**, 11449–11456.
163 J. Liu, D. J. Van Hoomissen, T. Liu, A. Maizel, X. Huo, S. R. Fernández, C. Ren, X. Xiao, Y. Fang, C. E. Schaefer, C. P. Higgins, S. Vyas and T. J. Strathmann, *Environ. Sci. Technol. Lett.*, 2018, **5**, 289–294.
164 J. F. King and B. P. Chaplin, *Curr. Opin. Chem. Eng.*, 2024, **44**, 101014.
165 H. Wu, J. Wang, E. Du, T. Liu, M. Liu, H. Guo and W. Chu, *Water Res.*, 2025, **279**, 123499.
166 M. Zhang, Y. Li, X. Tian, L. Dai, G. Wang, Z. Lei, G. Ma, Q. Zuo, M. Li, M. Zhao and J. Ren, *Water, Air, Soil Pollut.*, 2024, **236**, 42.
167 L. Saleh, Z. Lin, M. S. Ersan, C. Coutanceau, P. Westerhoff and J.-P. Croué, *Chemosphere*, 2024, **363**, 142879.
168 H. Ma, G. Kong, C. Chen, Z. Guo, J. Huang, S. Kuang, J. Zhang and Y. Kang, *Water Res.*, 2025, **277**, 123302.
169 F. A. Zeidabadi, P. Abbasi, E. B. Esfahani and M. Mohseni, *J. Hazard. Mater.*, 2025, **484**, 136624.
170 C. B. Ong, A. W. Mohammad, L. Y. Ng, E. Mahmoudi, S. Azizkhani and N. H. Hayati Hairom, *Process Saf. Environ. Prot.*, 2017, **112**, 298–307.
171 M. M. Mian, J. Zhu, X. Jiang and S. Deng, *Front. Environ. Sci. Eng.*, 2025, **19**, 2095–2201.
172 M. Priyadarshini, A. Ahmad, M. S. Mahtab, S. U. Khan, I. H. Farooqi and N. Pérez, *Groundw. Sustain. Dev.*, 2025, **30**, 101465.
173 C. Chen, Q. Ma, F. Liu, J. Gao, X. Li, S. Sun, H. Yao, C. Liu, J. Young and W. Zhang, *J. Hazard. Mater.*, 2021, **419**, 126452.
174 A. Yousefi, F. R. Omi, L. Yang, S. O. Ganiyu, A. Ullah, M. G. El-Din and M. Sadrzadeh, *J. Environ. Manage.*, 2025, **379**, 124818.
175 A. Román Santiago, P. Baldaguez Medina and X. Su, *Electrochim. Acta*, 2022, **403**, 139635.
176 Z. Wan, L. Cao, W. Huang, D. Zheng, G. Li and F. Zhang, *Environ. Sci. Technol. Lett.*, 2022, **10**, 111–116.
177 H. Shi, S.-Y. Chiang, Y. Wang, Y. Wang, S. Liang, J. Zhou, R. Fontanez, S. Gao and Q. Huang, *Sci. Total Environ.*, 2021, **788**, 147723.
178 Á. Soriano, D. Gorri and A. Urtiaga, *Water Res.*, 2017, **112**, 147–156.
179 A. P. Trzcinski and K. H. Harada, *Sci. Total Environ.*, 2024, **927**, 172184.
180 A. P. Trzcinski and K. Harada, *Chemosphere*, 2023, **323**, 138268.
181 H. D. Hieu Nhu, D. V. Tri, T. L. Luu, J. Trippel and M. Wagner, *Sep. Purif. Technol.*, 2025, **362**, 131908.
182 C. Gomri, E. Makhoul, F. N. Koundia, E. Petit, S. Raffy, M. Bechelany, M. Semsarilar and M. Cretin, *Nanoscale Adv.*, 2025, **7**, 261–268.

183 U. Rao, Y. Su, C. M. Khor, B. Jung, S. Ma, D. M. Cwiertny, B. M. Wong and D. Jassby, *Environ. Sci. Technol.*, 2020, **54**, 10668–10677.

184 Z. Meng, T. Taseska, M. K. Wilsey and A. M. Müller, *RSC Adv.*, 2025, **15**, 8287–8292.

185 A. P. Trzcinski and K. Harada, *Environ. Sci. Pollut. Res.*, 2024, **31**, 19946–19960.

186 K. Kim, P. Baldaguez Medina, J. Elbert, E. Kayiwa, R. D. Cusick, Y. Men and X. Su, *Adv. Funct. Mater.*, 2020, **30**, 2004635.